Geophysical Journal International

Geophys. J. Int. (2011) **185,** 1335–1364 doi: 10.1111/j.1365-246X.2011.05007.x

Seismic interferometry by crosscorrelation and by multidimensional deconvolution: a systematic comparison

Kees Wapenaar,[1] Joost van der Neut,[1] Elmer Ruigrok,[1] Deyan Draganov,[1] Jürg Hunziker,[1] Evert Slob,[1] Jan Thorbecke[1] and Roel Snieder[2]

[1] *Department of Geotechnology, Delft University of Technology, P.O. Box* 5048, 2600 *GA Delft, The Netherlands. E-mail: c.p.a.wapenaar@tudelft.nl*
[2] *Center for Wave Phenomena, Colorado School of Mines, Golden, Colorado* 80401, *USA*

Accepted 2011 March 2. Received 2011 February 16; in original form 2010 August 11

SUMMARY

Seismic interferometry, also known as Green's function retrieval by crosscorrelation, has a wide range of applications, ranging from surface-wave tomography using ambient noise, to creating virtual sources for improved reflection seismology. Despite its successful applications, the crosscorrelation approach also has its limitations. The main underlying assumptions are that the medium is lossless and that the wavefield is equipartitioned. These assumptions are in practice often violated: the medium of interest is often illuminated from one side only, the sources may be irregularly distributed, and losses may be significant. These limitations may partly be overcome by reformulating seismic interferometry as a multidimensional deconvolution (MDD) process. We present a systematic analysis of seismic interferometry by crosscorrelation and by MDD. We show that for the non-ideal situations mentioned above, the correlation function is proportional to a Green's function with a blurred source. The source blurring is quantified by a so-called interferometric point-spread function which, like the correlation function, can be derived from the observed data (i.e. without the need to know the sources and the medium). The source of the Green's function obtained by the correlation method can be deblurred by deconvolving the correlation function for the point-spread function. This is the essence of seismic interferometry by MDD. We illustrate the crosscorrelation and MDD methods for controlled-source and passive-data applications with numerical examples and discuss the advantages and limitations of both methods.

Key words: Inverse theory; Interferometry; Body waves; Surface waves and free oscillations; Coda waves; Wave scattering and diffraction.

1 INTRODUCTION

In recent years, the methodology of Green's function retrieval by crosscorrelation has led to many applications in seismology (exploration, regional and global), underwater acoustics and ultrasonics. In seismology this methodology is also called 'seismic interferometry'. One of the explanations for the broad interest lies in the fact that new responses can be obtained from measured data in a very simple way. In passive-data applications, a straightforward crosscorrelation of responses at two receivers gives the impulse response (Green's function) at one receiver of a virtual source at the position of the other. In controlled-source applications the procedure is similar, except that it involves in addition a summation over the sources. For a review of the theory and the many applications of seismic interferometry, see Larose *et al.* (2006), Schuster (2009) and Snieder *et al.* (2009).

It has also been recognized that the simple crosscorrelation approach has its limitations. From the various theoretical models it follows that there is a number of underlying assumptions for retrieving the Green's function by crosscorrelation. The most important assumptions are that the medium is lossless and that the waves are equipartitioned. In heuristic terms, the latter condition means that the receivers are illuminated isotropically from all directions, which is for example, achieved when the sources are regularly distributed along a closed surface, the sources are mutually uncorrelated and their power spectra are identical. Despite the fact that in practical situations these conditions are at most only partly fulfilled, the results of seismic interferometry are generally quite robust, but the retrieved amplitudes are unreliable and the results are often blurred by artefacts.

Several researchers have proposed to address some of the shortcomings by replacing the correlation process by deconvolution. In the 'virtual source method', pioneered by Bakulin & Calvert (2004), the main limitation is that the real sources are present only at the Earth's

surface, that is, above the downhole receivers, instead of on a closed surface surrounding the receivers, as prescribed by the theory (Wapenaar *et al.* 2005; van Manen *et al.* 2005; Korneev & Bakulin 2006). To compensate for this one-sided illumination, Bakulin & Calvert (2006) propose to replace the correlation by a deconvolution for the downgoing wavefield at the downhole receivers. They show that this approach compensates for variations in the source wavelet and, partly, for reverberations in the overburden. Snieder *et al.* (2006a) deconvolve passive wavefields observed at different depth levels and show that, apart from compensating for the source function, this methodology also changes the boundary conditions of the system. They applied it to earthquake data recorded at different heights in the Millikan library in Pasadena and obtained the impulse response of the building. Mehta *et al.* (2007b) used a similar approach to estimate the near-surface properties of the Earth from passive recordings in a vertical borehole. Vasconcelos & Snieder (2008a,b) and Vasconcelos *et al.* (2008) used deconvolution interferometry in seismic imaging with complicated and unknown source-time signals and for imaging with internal multiples. All these approaches improve seismic interferometry to some extent. An important positive aspect is that the required processing in all these cases is not much more complicated than in the correlation approach because the employed deconvolution procedures are essentially 1-D (i.e. trace-by-trace deconvolution). This compensates for variations in the source wavelet, anelastic losses and, partly, for internal multiples, but it does not account for the anisotropic illumination of the receivers.

To obtain more accurate results, seismic interferometry by deconvolution should acknowledge the 3-D nature of the seismic wavefield. Hence, from a theoretical point of view, the trace-by-trace deconvolution process should be replaced by a full 3-D wavefield deconvolution process. In the following we speak of multidimensional deconvolution (MDD), which stands for 3-D wavefield deconvolution in the 3-D situation, or for 2-D wavefield deconvolution in the 2-D situation. The MDD principle is not entirely new. It has been applied for example, for multiple elimination of ocean-bottom data (Wapenaar *et al.* 2000; Amundsen 2001). Like the aforementioned method of Snieder *et al.* (2006a), this can be seen as a methodology that changes the boundary conditions of the system: it transforms the response of the subsurface including the effects of the reflecting ocean bottom and water surface into the response of a subsurface without these reflecting boundaries. With hindsight this methodology appears to be an extension of a 1-D deconvolution approach proposed by Riley & Claerbout (1976). Muijs *et al.* (2007) employ multidimensional deconvolution for the downgoing wavefield (including multiples) in the imaging condition, thus improving the illumination and resolution of the imaged structures. Schuster & Zhou (2006) and Wapenaar *et al.* (2008a) discuss MDD of controlled-source data in the context of seismic interferometry. Slob *et al.* (2007) apply MDD to modelled controlled-source electromagnetic (CSEM) data and demonstrate the relative insensitivity to dissipation as well as the potential of changing the boundary conditions: the effect of the air wave, a notorious problem in CSEM prospecting, is largely suppressed. Wapenaar *et al.* (2008b) apply MDD to passive seismic data and show how it corrects for anisotropic illumination due to an irregular source distribution. Van der Neut & Bakulin (2009) show how MDD can be used to improve the radiation pattern of a virtual source. In a related method, called 'directional balancing', Curtis & Halliday (2010) deconvolve the crosscorrelation result by the estimated radiation pattern of the virtual source.

Interferometry by MDD is more accurate than the trace-by-trace correlation and deconvolution approaches but the processing is more involved. In this paper, we present a systematic analysis of seismic interferometry by crosscorrelation versus multidimensional deconvolution and discuss applications of both approaches.

2 GREEN'S FUNCTION REPRESENTATIONS FOR SEISMIC INTERFEROMETRY

We briefly review two Green's function representations for seismic interferometry. Consider a volume $\mathbb{V}$ enclosed by a surface $\mathbb{S}$, with outward pointing normal vector $\mathbf{n} = (n_1, n_2, n_3)$. In $\mathbb{V}$ we have an arbitrary inhomogeneous medium with acoustic propagation velocity $c(\mathbf{x})$ and mass density $\rho(\mathbf{x})$ (where $\mathbf{x} = (x_1, x_2, x_3)$ is the Cartesian coordinate vector). We consider two points in $\mathbb{V}$ denoted by coordinate vectors $\mathbf{x}_A$ and $\mathbf{x}_B$, see Fig. 1(a). We define the Fourier transform of a time-dependent function $u(t)$ as $\hat{u}(\omega) = \int_{-\infty}^{\infty} \exp(-j\omega t)u(t)\,\mathrm{d}t$, with j the imaginary unit and ω the angular frequency. Assuming the medium in $\mathbb{V}$ is lossless, the correlation-type representation for the acoustic Green's function between $\mathbf{x}_A$ and $\mathbf{x}_B$ in $\mathbb{V}$ reads (Wapenaar *et al.* 2005; van Manen *et al.* 2005)

$$\hat{\bar{G}}(\mathbf{x}_B, \mathbf{x}_A, \omega) + \hat{G}^*(\mathbf{x}_B, \mathbf{x}_A, \omega) = -\oint_{\mathbb{S}} \frac{1}{j\omega\rho(\mathbf{x})}\Big(\partial_i \hat{\bar{G}}(\mathbf{x}_B, \mathbf{x}, \omega)\hat{G}^*(\mathbf{x}_A, \mathbf{x}, \omega) - \hat{\bar{G}}(\mathbf{x}_B, \mathbf{x}, \omega)\partial_i \hat{G}^*(\mathbf{x}_A, \mathbf{x}, \omega)\Big)n_i\,\mathrm{d}\mathbf{x} \tag{1}$$

(Einstein's summation convention applies to repeated lower case Latin subscripts). This representation is a basic expression for seismic interferometry (or Green's function retrieval) by crosscorrelation in open systems. The superscript asterisk * denotes complex conjugation, hence, the products on the right-hand side correspond to crosscorrelations in the time domain of observations at two receivers at $\mathbf{x}_A$ and $\mathbf{x}_B$. The notation $\hat{\bar{G}}$ is introduced to denote a reference state with possibly different boundary conditions at $\mathbb{S}$ and/or different medium parameters outside $\mathbb{S}$ (but in $\mathbb{V}$ the medium parameters for $\hat{\bar{G}}$ are the same as those for $\hat{G}$). The bar is usually omitted because $\hat{G}$ and $\hat{\bar{G}}$ are usually defined in the same medium throughout space. The Green's functions on the left-hand side are the Fourier transforms of the response of a source at $\mathbf{x}_A$ observed at $\mathbf{x}_B$ and its time-reversed version. Representation (1) is exact, hence, it accounts not only for the direct wave, but also for primary and multiply scattered waves. Note that the inverse Fourier transform of the left-hand side gives $\bar{G}(\mathbf{x}_B, \mathbf{x}_A, t) + G(\mathbf{x}_B, \mathbf{x}_A, -t)$, from which $\bar{G}(\mathbf{x}_B, \mathbf{x}_A, t)$ and $G(\mathbf{x}_B, \mathbf{x}_A, -t)$ can be obtained by extracting the causal and acausal part, respectively. Porter (1970), Esmersoy & Oristaglio (1988) and Oristaglio (1989) used an expression similar to equation (1) (without the bars) in optical holography, seismic migration

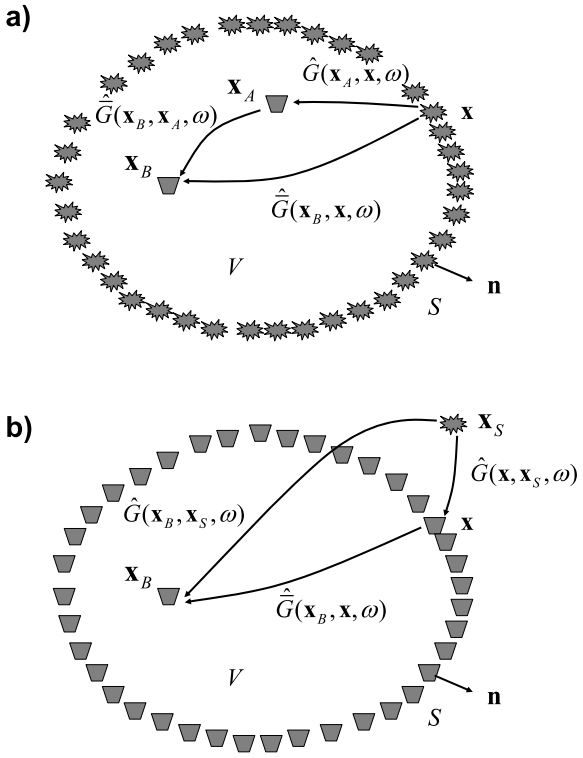

Figure 1. (a) Configuration for the correlation-type Green's function representation (eq. 1). The medium in $\mathbb{V}$ is assumed lossless. The rays represent full responses, including primary and multiple scattering due to inhomogeneities inside as well as outside $\mathbb{S}$. The bar in $\bar{\hat{G}}$ refers to a reference state with possibly different boundary conditions at $\mathbb{S}$ and/or different medium parameters outside $\mathbb{S}$ (in $\mathbb{V}$ the medium parameters are the same for $\hat{G}$ and $\bar{\hat{G}}$). (b) Configuration for the convolution-type Green's function representation (eq. 2). Here the medium does not need to be lossless.

and acoustic inverse scattering, respectively, see Thorbecke & Wapenaar (2007) and Halliday & Curtis (2010) for a further discussion on the relation between these different applications of eq. (1).

Next, we consider a convolution-type representation for the Green's function. We slightly modify the configuration by taking $\mathbf{x}_A$ outside $\mathbb{S}$ and renaming it $\mathbf{x}_S$, see Fig. 1(b). For this configuration the convolution-type representation is given by

$$\hat{G}(\mathbf{x}_B, \mathbf{x}_S, \omega) = -\oint_{\mathbb{S}} \frac{1}{j\omega\rho(\mathbf{x})}\Big(\partial_i \bar{\hat{G}}(\mathbf{x}_B, \mathbf{x}, \omega)\hat{G}(\mathbf{x}, \mathbf{x}_S, \omega) - \bar{\hat{G}}(\mathbf{x}_B, \mathbf{x}, \omega)\partial_i \hat{G}(\mathbf{x}, \mathbf{x}_S, \omega)\Big)n_i \, \mathrm{d}\mathbf{x}. \tag{2}$$

Due to the absence of complex-conjugation signs, the products on the right-hand side correspond to crossconvolutions in the time domain. An important difference with the correlation-type representation is that this representation remains valid in media with losses. Again, the bar in $\bar{\hat{G}}$ refers to a reference state with possibly different boundary conditions at $\mathbb{S}$ and/or different medium parameters outside $\mathbb{S}$. Slob & Wapenaar (2007) use the electromagnetic equivalent of eq. (2) (without the bars) as the starting point for interferometry by crossconvolution in lossy media. A discussion of interferometry by crossconvolution is beyond the scope of this paper. We will use eq. (2) as the starting point for interferometry by deconvolution in open systems. By considering $\bar{\hat{G}}(\mathbf{x}_B, \mathbf{x}, \omega)$ under the integral as the unknown quantity, eq. (2) needs to be resolved by multidimensional deconvolution.

3 BASIC ASPECTS OF INTERFEROMETRY BY CROSSCORRELATION

3.1 Simplification of the integral

The correlation-type Green's function representation (eq. 1) is a basic expression for seismic interferometry by crosscorrelation in open systems. The right-hand side of this equation contains a combination of two correlation products. We show how we can combine these two terms into a single term. To this end, we assume that the medium at and outside $\mathbb{S}$ is homogeneous, with constant propagation velocity c and mass density ρ, for $\hat{G}$ as well as for $\bar{\hat{G}}$. In other words, $\mathbb{S}$ is an absorbing boundary for $\hat{G}$ and $\bar{\hat{G}}$. Because the boundary conditions are the same, we drop the bar in $\bar{\hat{G}}$ in the remainder of this section. Assuming $\mathbb{S}$ is sufficiently smooth, the normal differential operator $n_i\partial_i$ acting on the Green's functions can be replaced by a pseudo-differential operator $-j\hat{\mathcal{H}}_1$, where $\hat{\mathcal{H}}_1$ is the square-root of the Helmholtz operator defined on curvilinear coordinates along $\mathbb{S}$. For details about this operator we refer to Fishman & McCoy (1984), Wapenaar & Berkhout

(1989, appendix B), Fishman (1993) and Frijlink & Wapenaar (2010). Hence, for the integral in eq. (1) we may write

$$\oint_{\mathbb{S}}\Big((\partial_i\hat{G}_B)\hat{G}^*_A-\hat{G}_B(\partial_i\hat{G}^*_A)\Big)n_i\,\mathrm{d}\mathbf{x}=\oint_{\mathbb{S}}\Big((-j\hat{\mathcal{H}}_1\hat{G}_B)\hat{G}^*_A-\hat{G}_B(j\hat{\mathcal{H}}_1^*\hat{G}^*_A)\Big)\,\mathrm{d}\mathbf{x}=\oint_{\mathbb{S}}\Big(-j(\hat{\mathcal{H}}_1+\hat{\mathcal{H}}_1^*)\hat{G}_B\Big)\hat{G}^*_A\,\mathrm{d}\mathbf{x},\tag{3}$$

where we used the fact that $\hat{\mathcal{H}}_1$ is symmetric [in the sense that $\oint(\hat{\mathcal{H}}_1 f)g\,\mathrm{d}\mathbf{x}=\oint f(\hat{\mathcal{H}}_1 g)\,\mathrm{d}\mathbf{x}$]. Note that $\hat{G}_A$ and $\hat{G}_B$ stand for $\hat{G}(\mathbf{x}_A,\mathbf{x},\omega)$ and $\hat{G}(\mathbf{x}_B,\mathbf{x},\omega)$, respectively. Zheng (2010) and Zheng *et al.* (2011) evaluate the kernel of $-j(\hat{\mathcal{H}}_1+\hat{\mathcal{H}}_1^*)$ analytically for a number of special cases and show that in theory the last integral in eq. (3) may lead to an exact retrieval of the Green's function. For most practical applications some further approximations need to be made. If we ignore the contribution of evanescent waves, we may approximate $\hat{\mathcal{H}}_1^*$ by $\hat{\mathcal{H}}_1$, hence

$$\oint_{\mathbb{S}}\Big(-j(\hat{\mathcal{H}}_1+\hat{\mathcal{H}}_1^*)\hat{G}_B\Big)\hat{G}^*_A\,\mathrm{d}\mathbf{x}\approx 2\oint_{\mathbb{S}}(-j\hat{\mathcal{H}}_1\hat{G}_B)\hat{G}^*_A\,\mathrm{d}\mathbf{x}=2\oint_{\mathbb{S}}(n_i\partial_i\hat{G}_B)\hat{G}^*_A\,\mathrm{d}\mathbf{x}.\tag{4}$$

Using eqs (3) and (4) in eq. (1) and rewriting $\mathbf{x}$ as $\mathbf{x}_S$ (standing for the source coordinate vector), we obtain

$$\hat{G}(\mathbf{x}_B,\mathbf{x}_A,\omega)+\hat{G}^*(\mathbf{x}_B,\mathbf{x}_A,\omega)=-\frac{2}{j\omega\rho}\oint_{\mathbb{S}_{\mathrm{src}}}\big(n_i\partial_i^S\hat{G}(\mathbf{x}_B,\mathbf{x}_S,\omega)\big)\hat{G}^*(\mathbf{x}_A,\mathbf{x}_S,\omega)\,\mathrm{d}\mathbf{x}_S,\tag{5}$$

where the superscript S in ∂_i^S denotes that the differentiation is carried out with respect to the components of $\mathbf{x}_S$. Note that we added a subscript 'src' in $\mathbb{S}_{\mathrm{src}}$ to denote that the integration surface contains the sources of the Green's functions. The integrand of eq. (5) contains a single crosscorrelation product of dipole and monopole source responses. When only monopole responses are available, the operation $n_i\partial_i^S$ can be replaced by the pseudo-differential operator $-j\hat{\mathcal{H}}_1$ acting along $\mathbb{S}_{\mathrm{src}}$, or in the high-frequency approximation by multiplications with $-jk\,|\cos\alpha|$, where $k=\omega/c$, and α is the angle between the relevant ray and the normal on $\mathbb{S}$. Hence, for controlled-source interferometry, in which case the source positions are known and $\mathbb{S}_{\mathrm{src}}$ is usually a smooth surface, eq. (5) is a useful expression. In passive interferometry, the positions of the sources are unknown and $\mathbb{S}_{\mathrm{src}}$ can be very irregular. In that case, the best one can do is replace the operation $n_i\partial_i^S$ by a factor $-jk$, which leads to

$$\hat{G}(\mathbf{x}_B,\mathbf{x}_A,\omega)+\hat{G}^*(\mathbf{x}_B,\mathbf{x}_A,\omega)\approx\frac{2}{\rho c}\oint_{\mathbb{S}_{\mathrm{src}}}\hat{G}(\mathbf{x}_B,\mathbf{x}_S,\omega)\hat{G}^*(\mathbf{x}_A,\mathbf{x}_S,\omega)\,\mathrm{d}\mathbf{x}_S.\tag{6}$$

Eq. (6) is accurate when $\mathbb{S}_{\mathrm{src}}$ is a sphere with a very large radius, but it involves amplitude errors when $\mathbb{S}_{\mathrm{src}}$ is finite. Moreover, spurious events may occur due to incomplete cancelation of contributions from different stationary points. However, since the approximation does not affect the phase, eq. (6) is usually considered acceptable for seismic interferometry. Note that for a modified Green's function $\hat{\mathcal{G}}=\hat{G}/j\omega$ we have, instead of eq. (6),

$$\hat{\mathcal{G}}(\mathbf{x}_B,\mathbf{x}_A,\omega)-\hat{\mathcal{G}}^*(\mathbf{x}_B,\mathbf{x}_A,\omega)\approx-\frac{2j\omega}{\rho c}\oint_{\mathbb{S}_{\mathrm{src}}}\hat{\mathcal{G}}(\mathbf{x}_B,\mathbf{x}_S,\omega)\hat{\mathcal{G}}^*(\mathbf{x}_A,\mathbf{x}_S,\omega)\,\mathrm{d}\mathbf{x}_S\tag{7}$$

(Wapenaar & Fokkema 2006). Both eqs (6) and (7) are used in the literature on seismic interferometry. Because of the simple relation between $\hat{G}$ and $\hat{\mathcal{G}}$, these equations are completely interchangeable. In the following we continue with eq. (6). In the time domain this equation reads

$$G(\mathbf{x}_B,\mathbf{x}_A,t)+G(\mathbf{x}_B,\mathbf{x}_A,-t)\approx\frac{2}{\rho c}\oint_{\mathbb{S}_{\mathrm{src}}}G(\mathbf{x}_B,\mathbf{x}_S,t)*G(\mathbf{x}_A,\mathbf{x}_S,-t)\,\mathrm{d}\mathbf{x}_S.\tag{8}$$

The in-line asterisk $*$ denotes temporal convolution, but the time-reversal of the second Green's function turns the convolution into a correlation. Eq. (8) shows that the crosscorrelation of two Green's functions observed by receivers at $\mathbf{x}_A$ and $\mathbf{x}_B$, followed by an integration along the sources, gives the Green's function between $\mathbf{x}_A$ and $\mathbf{x}_B$ plus its time-reversed version.

3.2 Transient and noise sources

For practical situations the Green's functions in the right-hand side of eq. (8) should be replaced by responses of real sources, that is, Green's functions convolved with source functions. When the source functions are transients, $s(\mathbf{x}_S,t)$, we write for the responses at $\mathbf{x}_A$ and $\mathbf{x}_B$

$$u(\mathbf{x}_A,\mathbf{x}_S,t)=G(\mathbf{x}_A,\mathbf{x}_S,t)*s(\mathbf{x}_S,t),\tag{9}$$

$$u(\mathbf{x}_B,\mathbf{x}_S,t)=G(\mathbf{x}_B,\mathbf{x}_S,t)*s(\mathbf{x}_S,t).\tag{10}$$

For this situation, we define a correlation function $C(\mathbf{x}_B,\mathbf{x}_A,t)$ as

$$C(\mathbf{x}_B,\mathbf{x}_A,t)=\oint_{\mathbb{S}_{\mathrm{src}}}\mathcal{F}(\mathbf{x}_S,t)*u(\mathbf{x}_B,\mathbf{x}_S,t)*u(\mathbf{x}_A,\mathbf{x}_S,-t)\,\mathrm{d}\mathbf{x}_S,\tag{11}$$

where $\mathcal{F}(\mathbf{x}_S,t)$ is a filter that compensates for the variations of the autocorrelation of the source function, in such a way that

$$\mathcal{F}(\mathbf{x}_S,t)*s(\mathbf{x}_S,t)*s(\mathbf{x}_S,-t)=S(t),\tag{12}$$

where $S(t)$ is some (arbitrarily chosen) average autocorrelation. Substituting eqs (9) and (10) into eq. (11), using eq. (12), and comparing the result with eq. (8) gives

$$\{G(\mathbf{x}_B,\mathbf{x}_A,t)+G(\mathbf{x}_B,\mathbf{x}_A,-t)\}*S(t)\approx\frac{2}{\rho c}\,C(\mathbf{x}_B,\mathbf{x}_A,t).\tag{13}$$

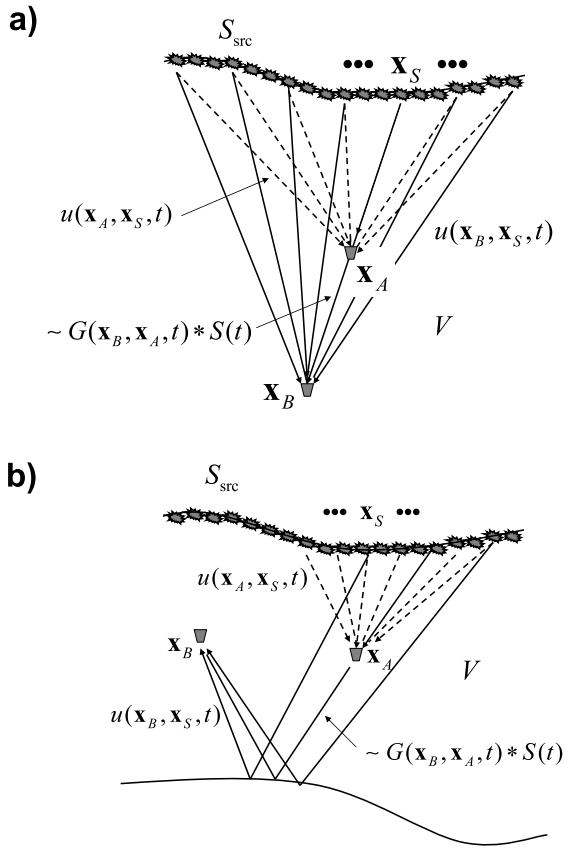

Figure 2. (a) Illustration of interferometry by crosscorrelation [eqs (11) and (13)] for the situation of direct-wave interferometry. The responses $u(\mathbf{x}_A, \mathbf{x}_S, t)$ and $u(\mathbf{x}_B, \mathbf{x}_S, t)$ are crosscorrelated and the results for all sources $\mathbf{x}_S$ are integrated along the source boundary $\mathbb{S}_{\text{src}}$. The correlation function is approximately proportional to $G(\mathbf{x}_B, \mathbf{x}_A, t) * S(t)$. (b) Idem, for reflected-wave interferometry.

When the source functions are simultaneously acting noise signals, $N(\mathbf{x}_S, t)$, the responses at $\mathbf{x}_A$ and $\mathbf{x}_B$ are given by

$$u(\mathbf{x}_A, t) = \oint_{\mathbb{S}_{\text{src}}} G(\mathbf{x}_A, \mathbf{x}_S, t) * N(\mathbf{x}_S, t)\ \mathrm{d}\mathbf{x}_S, \tag{14}$$

$$u(\mathbf{x}_B, t) = \oint_{\mathbb{S}_{\text{src}}} G(\mathbf{x}_B, \mathbf{x}'_S, t) * N(\mathbf{x}'_S, t)\ \mathrm{d}\mathbf{x}'_S. \tag{15}$$

We assume that two noise sources $N(\mathbf{x}_S, t)$ and $N(\mathbf{x}'_S, t)$ are mutually uncorrelated for any $\mathbf{x}_S \neq \mathbf{x}'_S$ on $\mathbb{S}_{\text{src}}$ and that their autocorrelations are independent of $\mathbf{x}_S$. Hence, we assume that these noise sources obey the relation

$$\langle N(\mathbf{x}'_S, t) * N(\mathbf{x}_S, -t)\rangle = \delta(\mathbf{x}_S - \mathbf{x}'_S)S(t), \tag{16}$$

where $\langle\cdot\rangle$ denotes ensemble averaging and $S(t)$ the autocorrelation of the noise. Note that $\delta(\mathbf{x}_S - \mathbf{x}'_S)$ is defined for $\mathbf{x}_S$ and $\mathbf{x}'_S$ both on $\mathbb{S}_{\text{src}}$. This time we define the correlation function as

$$C(\mathbf{x}_B, \mathbf{x}_A, t) = \langle u(\mathbf{x}_B, t) * u(\mathbf{x}_A, -t)\rangle. \tag{17}$$

In practice, the ensemble averaging is replaced by integrating over sufficiently long time and/or averaging over different time intervals. Substituting eqs (14) and (15) into eq. (17), using eq. (16), and comparing the result with eq. (8) gives again eq. (13). Hence, whether we consider transient or noise sources, eq. (13) states that a properly defined correlation function gives the Green's function plus its time-reversed version, convolved with the autocorrelation of the source function.

In most practical situations, sources are not available on a closed boundary. When a part of the integration boundary is a free surface, the integrals need only be evaluated over the remaining part of the boundary, hence, sources need only be available on an open boundary $\mathbb{S}_{\text{src}}$ that, together with the free surface, forms a closed boundary. This situation occurs in passive reflected-wave interferometry (Section 6.2). In many other situations the closed source boundary is replaced by an open surface, simply because the available source aperture is restricted to an open boundary. This is illustrated in Fig. 2(a) for the situation of direct-wave interferometry and in Fig. 2(b) for controlled-source reflected-wave interferometry (these configurations will be discussed in more detail in Sections 6.1 and 5.1, respectively). Since the underlying representation (eq. 1) is of the correlation type (in which one of the Green's functions is backward propagating), radiation conditions do not apply anywhere on $\mathbb{S}$, hence, replacing the closed surface by an open surface necessarily leads to approximations. For the situation of

direct-wave interferometry (Fig. 2a) the main effect is that the correlation function $C(\mathbf{x}_B, \mathbf{x}_A, t)$ is approximately proportional to $G(\mathbf{x}_B, \mathbf{x}_A, t) * S(t)$, that is, the time-reversed version of the Green's function in eq. (13) is not recovered [see e.g. Sabra *et al.* (2005b) and Miyazawa *et al.* (2008)]. For reflected-wave interferometry (Fig. 2b), one-sided illumination can lead to severe distortions of the retrieved Green's function. Moreover, Snieder *et al.* (2006b) show that even for very simple configurations it may lead to spurious multiples. An important aspect of interferometry by MDD, discussed in the next section, is that the approximations of one-sided illumination are avoided in a natural way.

4 BASIC ASPECTS OF INTERFEROMETRY BY MULTIDIMENSIONAL DECONVOLUTION (MDD)

4.1 Simplification of the integral

The convolution-type Green's function representation (eq. 2) is a basic expression for seismic interferometry by multidimensional deconvolution in open systems. The right-hand side of this equation contains a combination of two convolution products. We show how we can combine these two terms into a single term. The Green's function $\hat{\tilde{G}}(\mathbf{x}_B, \mathbf{x}, \omega)$ under the integral is the unknown that we want to resolve by MDD. The Green's function $\hat{G}(\mathbf{x}_B, \mathbf{x}_S, \omega)$ on the left-hand side and $\hat{G}(\mathbf{x}, \mathbf{x}_S, \omega)$ under the integral are related to the observations. Hence, $\hat{G}$ is defined in the actual medium inside as well as outside $\mathbb{S}$, but for $\hat{\tilde{G}}$ we are free to choose convenient boundary conditions at $\mathbb{S}$. In the following, we let $\mathbb{S}$ be an absorbing boundary for $\hat{\tilde{G}}(\mathbf{x}_B, \mathbf{x}, \omega)$, so that its reciprocal $\hat{\tilde{G}}(\mathbf{x}, \mathbf{x}_B, \omega)$ is outward propagating at $\mathbb{S}$. Furthermore, we write $\hat{G}(\mathbf{x}, \mathbf{x}_S, \omega)$ as the superposition of an inward- and outward-propagating part at $\mathbf{x}$ on $\mathbb{S}$, according to $\hat{G}(\mathbf{x}, \mathbf{x}_S, \omega) = \hat{G}^{\mathrm{in}}(\mathbf{x}, \mathbf{x}_S, \omega) + \hat{G}^{\mathrm{out}}(\mathbf{x}, \mathbf{x}_S, \omega)$. Assuming $\mathbb{S}$ is sufficiently smooth, we replace the differential operator $n_i\partial_i$ again by a pseudo-differential operator $\pm j\hat{\mathcal{H}}_1$, this time for a medium with losses (Wapenaar *et al.* 2001). The plus- and minus-sign in $\pm j\hat{\mathcal{H}}_1$ correspond to inward- and outward-propagating waves, respectively. Hence, we may write for the integral in eq. (2), using the fact that $\hat{\mathcal{H}}_1$ is symmetric,

$$\begin{aligned}\oint_{\mathbb{S}}\Big(\Big(\partial_i\hat{\tilde{G}}_B\Big)\Big(\hat{G}_S^{\mathrm{in}}+\hat{G}_S^{\mathrm{out}}\Big)-\hat{\tilde{G}}_B\partial_i\Big(\hat{G}_S^{\mathrm{in}}+\hat{G}_S^{\mathrm{out}}\Big)\Big)n_i\,\mathrm{d}\mathbf{x} &= \oint_{\mathbb{S}}\Big(\Big(-j\hat{\mathcal{H}}_1\hat{\tilde{G}}_B\Big)\Big(\hat{G}_S^{\mathrm{in}}+\hat{G}_S^{\mathrm{out}}\Big)-\hat{\tilde{G}}_Bj\hat{\mathcal{H}}_1\Big(\hat{G}_S^{\mathrm{in}}-\hat{G}_S^{\mathrm{out}}\Big)\Big)\,\mathrm{d}\mathbf{x}\\ &= 2\oint_{\mathbb{S}}\Big(-j\hat{\mathcal{H}}_1\hat{\tilde{G}}_B\Big)\hat{G}_S^{\mathrm{in}}\,\mathrm{d}\mathbf{x}\\ &= 2\oint_{\mathbb{S}}\Big(n_i\partial_i\hat{\tilde{G}}_B\Big)\hat{G}_S^{\mathrm{in}}\,\mathrm{d}\mathbf{x},\end{aligned}\tag{18}$$

where $\hat{G}_S^{\mathrm{in/out}}$ and $\hat{\tilde{G}}_B$ stand for $\hat{G}^{\mathrm{in/out}}(\mathbf{x}, \mathbf{x}_S, \omega)$ and $\hat{\tilde{G}}(\mathbf{x}, \mathbf{x}_B, \omega) = \hat{\tilde{G}}(\mathbf{x}_B, \mathbf{x}, \omega)$, respectively.

Using this in eq. (2), assuming ρ is constant on $\mathbb{S}$, we obtain

$$\hat{G}(\mathbf{x}_B, \mathbf{x}_S, \omega) = \frac{-2}{j\omega\rho}\oint_{\mathbb{S}_{\mathrm{rec}}}\big(n_i\partial_i\hat{\tilde{G}}(\mathbf{x}_B, \mathbf{x}, \omega)\big)\hat{G}^{\mathrm{in}}(\mathbf{x}, \mathbf{x}_S, \omega)\,\mathrm{d}\mathbf{x}.\tag{19}$$

We added a subscript 'rec' in $\mathbb{S}_{\mathrm{rec}}$ to denote that the integration surface contains the receivers of the Green's function $\hat{G}^{\mathrm{in}}$. For convenience we introduce a dipole Green's function, defined as

$$\hat{\tilde{G}}_{\mathrm{d}}(\mathbf{x}_B, \mathbf{x}, \omega) = \frac{-2}{j\omega\rho}\big(n_i\partial_i\hat{\tilde{G}}(\mathbf{x}_B, \mathbf{x}, \omega)\big),\tag{20}$$

so that eq. (19) simplifies to

$$\hat{G}(\mathbf{x}_B, \mathbf{x}_S, \omega) = \oint_{\mathbb{S}_{\mathrm{rec}}}\hat{\tilde{G}}_{\mathrm{d}}(\mathbf{x}_B, \mathbf{x}, \omega)\hat{G}^{\mathrm{in}}(\mathbf{x}, \mathbf{x}_S, \omega)\,\mathrm{d}\mathbf{x}.\tag{21}$$

In the underlying representation (eq. 2) it was assumed that $\mathbf{x}_B$ lies in $\mathbb{V}$. In several applications of MDD $\mathbf{x}_B$ is a receiver on $\mathbb{S}_{\mathrm{rec}}$. For those applications, we take $\mathbf{x}_B$ just inside $\mathbb{S}_{\mathrm{rec}}$ to avoid several subtleties of taking $\mathbf{x}_B$ on $\mathbb{S}_{\mathrm{rec}}$. Moreover, in those applications it is often useful to consider only the outward-propagating part of the field at $\mathbf{x}_B$. Applying decomposition at both sides of eq. (21) gives

$$\hat{G}^{\mathrm{out}}(\mathbf{x}_B, \mathbf{x}_S, \omega) = \oint_{\mathbb{S}_{\mathrm{rec}}}\hat{\tilde{G}}_{\mathrm{d}}^{\mathrm{out}}(\mathbf{x}_B, \mathbf{x}, \omega)\hat{G}^{\mathrm{in}}(\mathbf{x}, \mathbf{x}_S, \omega)\,\mathrm{d}\mathbf{x}.\tag{22}$$

Eq. (22) is nearly the same (except for a different normalization) as our previously derived one-way representation for MDD (Wapenaar *et al.* 2008a). In the following, we continue with the notation of eq. (21), where $\hat{G}(\mathbf{x}_B, \mathbf{x}_S, \omega)$ and $\hat{\tilde{G}}_{\mathrm{d}}(\mathbf{x}_B, \mathbf{x}, \omega)$ may stand for the total or the outward-propagating fields at $\mathbf{x}_B$, depending on the application. In most practical situations, receivers are not available on a closed boundary, so the integration in eq. (21) is necessarily restricted to an open receiver boundary $\mathbb{S}_{\mathrm{rec}}$. As long as the source position $\mathbf{x}_S$ is located at the appropriate side of $\mathbb{S}_{\mathrm{rec}}$ (i.e., outside $\mathbb{V}$), it suffices to take the integral over the open receiver boundary: since the underlying representation (eq. 2) is of the convolution type, radiation conditions apply on the half-sphere that closes the boundary (assuming the half-sphere boundary is absorbing and its radius is sufficiently large), meaning that the contribution of the integral over that half-sphere vanishes. Hence, in the following we replace the closed boundary integral by an open boundary integral. In the time domain eq. (21) thus becomes

$$G(\mathbf{x}_B, \mathbf{x}_S, t) = \int_{\mathbb{S}_{\mathrm{rec}}}\tilde{G}_{\mathrm{d}}(\mathbf{x}_B, \mathbf{x}, t) * G^{\mathrm{in}}(\mathbf{x}, \mathbf{x}_S, t)\,\mathrm{d}\mathbf{x}.\tag{23}$$

Unlike the correlation-type representation (eq. 8), which holds under the condition that $\mathbb{S}_{\rm src}$ is a closed surface with very large radius, the convolution-type representation of eq. (23) holds as long as the open surface $\mathbb{S}_{\rm rec}$ is sufficiently smooth and $\mathbf{x}_B$ and $\mathbf{x}_S$ lie at opposite sides of $\mathbb{S}_{\rm rec}$. Moreover, whereas eq. (8) only holds for lossless media, eq. (23) also holds in media with losses. Eq. (23) is an implicit representation of the convolution type for $\bar{G}_{\rm d}(\mathbf{x}_B, \mathbf{x}, t)$. If it were a single equation, the inverse problem would be ill-posed. However, eq. (23) holds for each source position $\mathbf{x}_S$ (outside $\mathbb{V}$), which we will denote from hereon by $\mathbf{x}_S^{(i)}$, where i denotes the source number. Solving the ensemble of equations for $\bar{G}_{\rm d}(\mathbf{x}_B, \mathbf{x}, t)$ involves MDD.

4.2 Transient sources

For practical applications the Green's functions G and $G^{\rm in}$ in eq. (23) should be replaced by responses of real sources, that is, Green's functions convolved with source functions. For transient sources we may write for the responses at $\mathbf{x}$ and $\mathbf{x}_B$

$$u^{\rm in}\left(\mathbf{x}, \mathbf{x}_S^{(i)}, t\right) = G^{\rm in}\left(\mathbf{x}, \mathbf{x}_S^{(i)}, t\right) * s^{(i)}(t), \tag{24}$$

$$u\left(\mathbf{x}_B, \mathbf{x}_S^{(i)}, t\right) = G\left(\mathbf{x}_B, \mathbf{x}_S^{(i)}, t\right) * s^{(i)}(t). \tag{25}$$

Hence, by convolving both sides of eq. (23) with $s^{(i)}(t)$ we obtain

$$u\left(\mathbf{x}_B, \mathbf{x}_S^{(i)}, t\right) = \int_{\mathbb{S}_{\rm rec}} \bar{G}_{\rm d}(\mathbf{x}_B, \mathbf{x}, t) * u^{\rm in}\left(\mathbf{x}, \mathbf{x}_S^{(i)}, t\right)\, {\rm d}\mathbf{x}. \tag{26}$$

Here $u(\mathbf{x}_B, \mathbf{x}_S^{(i)}, t)$ and $\bar{G}_{\rm d}(\mathbf{x}_B, \mathbf{x}, t)$ may stand for the total or the outward-propagating fields at $\mathbf{x}_B$. We discuss the modifications for noise sources in Section 4.4 and for simultaneous source acquisition in Section 4.5.

Eq. (26) is illustrated in Fig. 3(a) for the situation of direct-wave interferometry and in Fig. 3(b) for reflected-wave interferometry (with superscripts 'out' added). Note that we consider the sources to be irregularly distributed in space. This is possible because eq. (26) holds for each source separately whereas the integration is performed along the receivers. The configurations in Figs 3(a) and (b) will be discussed in more detail in Sections 6.1 and 5, respectively.

Although in the derivation of eq. (26) we tacitly assumed a point source of volume injection rate at $\mathbf{x}_S^{(i)}$, eq. (26) holds equally well for other types of sources at $\mathbf{x}_S^{(i)}$, such as volume force or dislocation sources. The source also is not necessarily a point source. For an extended source, both sides of eq. (26) can be integrated along the extended source, yielding an equation with exactly the same form, but with $u^{\rm in}(\mathbf{x}, \mathbf{x}_S^{(i)}, t)$ and $u(\mathbf{x}_B, \mathbf{x}_S^{(i)}, t)$ being the responses of the extended source.

4.3 Relation with the correlation method

Solving eq. (26) in a least-squares sense is equivalent to solving its normal equation (Menke 1989). We obtain the normal equation by crosscorrelating both sides of eq. (26) with $u^{\rm in}(\mathbf{x}_A, \mathbf{x}_S^{(i)}, t)$ (with $\mathbf{x}_A$ on $\mathbb{S}_{\rm rec}$) and taking the sum over all sources (van der Neut *et al.* 2010). This gives

$$C(\mathbf{x}_B, \mathbf{x}_A, t) = \int_{\mathbb{S}_{\rm rec}} \bar{G}_{\rm d}(\mathbf{x}_B, \mathbf{x}, t) * \Gamma(\mathbf{x}, \mathbf{x}_A, t)\, {\rm d}\mathbf{x}, \tag{27}$$

where

$$\begin{aligned} C(\mathbf{x}_B, \mathbf{x}_A, t) &= \sum_i u\left(\mathbf{x}_B, \mathbf{x}_S^{(i)}, t\right) * u^{\rm in}(\mathbf{x}_A, \mathbf{x}_S^{(i)}, -t) \\ &= \sum_i G\left(\mathbf{x}_B, \mathbf{x}_S^{(i)}, t\right) * G^{\rm in}(\mathbf{x}_A, \mathbf{x}_S^{(i)}, -t) * S^{(i)}(t), \end{aligned} \tag{28}$$

$$\begin{aligned} \Gamma(\mathbf{x}, \mathbf{x}_A, t) &= \sum_i u^{\rm in}\left(\mathbf{x}, \mathbf{x}_S^{(i)}, t\right) * u^{\rm in}\left(\mathbf{x}_A, \mathbf{x}_S^{(i)}, -t\right) \\ &= \sum_i G^{\rm in}\left(\mathbf{x}, \mathbf{x}_S^{(i)}, t\right) * G^{\rm in}\left(\mathbf{x}_A, \mathbf{x}_S^{(i)}, -t\right) * S^{(i)}(t), \end{aligned} \tag{29}$$

with

$$S^{(i)}(t) = s^{(i)}(t) * s^{(i)}(-t). \tag{30}$$

Eq. (27) shows that the correlation function $C(\mathbf{x}_B, \mathbf{x}_A, t)$ is proportional to the sought Green's function $\bar{G}_{\rm d}(\mathbf{x}_B, \mathbf{x}, t)$ with its source smeared in space and time by $\Gamma(\mathbf{x}, \mathbf{x}_A, t)$.

Note that $C(\mathbf{x}_B, \mathbf{x}_A, t)$ as defined in eq. (28) is a correlation function with a similar form as the one defined in eq. (11). There are also some notable differences. In eq. (11) an integration takes place along the source boundary $\mathbb{S}_{\rm src}$, whereas eq. (28) involves a summation over individual sources. Of course in practical situations the integral in eq. (11) needs to be replaced by a summation as well, but this should be done carefully, obeying the common restrictions for discretization of continuous integrands. On the other hand, the summation in eq. (28) simply takes place over the available sources and as such puts no restrictions on the regularity of the source distribution. We will hold on

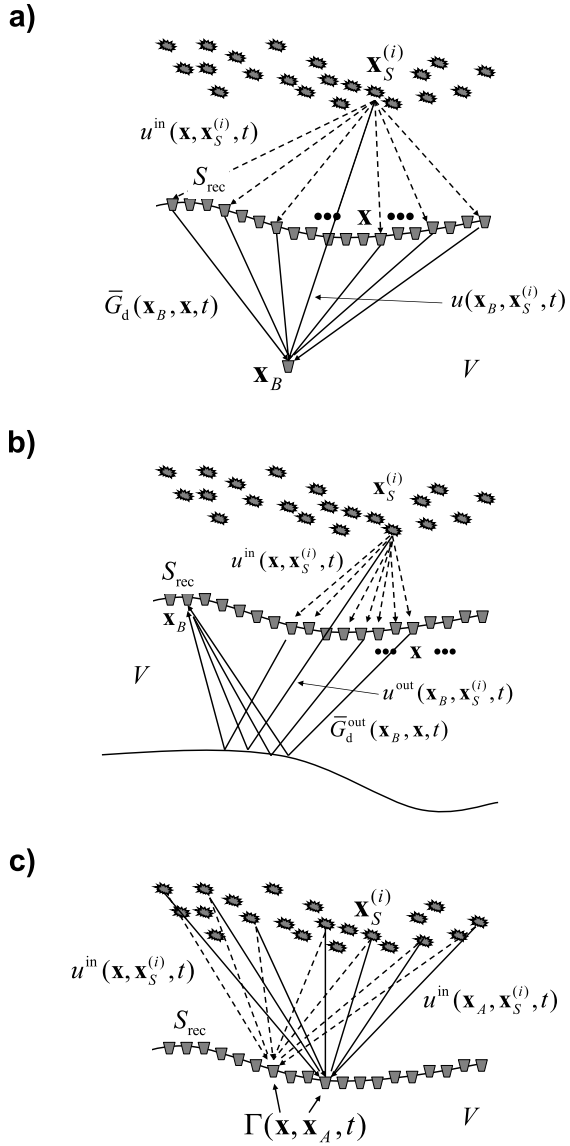

Figure 3. (a) Illustration of the convolutional model (eq. 26), underlying interferometry by MDD for the situation of direct-wave interferometry. The inward-propagating field $u^{\text{in}}(\mathbf{x}, \mathbf{x}_S^{(i)}, t)$ is convolved with $\bar{G}_{\text{d}}(\mathbf{x}_B, \mathbf{x}, t)$ and the results for all receivers $\mathbf{x}$ are integrated along the receiver boundary $\mathbb{S}_{\text{rec}}$, giving the response $u(\mathbf{x}_B, \mathbf{x}_S^{(i)}, t)$. Assuming eq. (26) is available for many source positions $\mathbf{x}_S^{(i)}$, the Green's function $\bar{G}_{\text{d}}(\mathbf{x}_B, \mathbf{x}, t)$ can be retrieved by MDD. (b) Idem, for reflected-wave interferometry, with $u(\mathbf{x}_B, \mathbf{x}_S^{(i)}, t)$ and $\bar{G}_{\text{d}}(\mathbf{x}_B, \mathbf{x}, t)$ replaced by the outgoing fields $u^{\text{out}}(\mathbf{x}_B, \mathbf{x}_S^{(i)}, t)$ and $\bar{G}_{\text{d}}^{\text{out}}(\mathbf{x}_B, \mathbf{x}, t)$, respectively. (c) Illustration of the point-spread function $\Gamma(\mathbf{x}, \mathbf{x}_A, t)$ (eq. 29), defined as the crosscorrelation of the inward-propagating fields at $\mathbf{x}$ and $\mathbf{x}_A$ on $\mathbb{S}_{\text{rec}}$, summed over the sources. In the ideal case, it is proportional to a band-limited delta function on $\mathbb{S}_{\text{rec}}$, but in practice there are many factors that make it different from a delta function.

to the integral notation in eq. (11) versus the summation notation in eq. (28) to express the differences in the assumptions on the regularity of the source distribution. The effect of this difference in assumptions will be illustrated in Sections 6.1 and 6.2. Another difference is that in eq. (11) the full wavefields at $\mathbf{x}_A$ and $\mathbf{x}_B$ are crosscorrelated, whereas in eq. (28) the inward-propagating part of the wavefield at $\mathbf{x}_A$ is crosscorrelated with the full (or outward-propagating) wavefield at $\mathbf{x}_B$. The final difference is the filter $\mathcal{F}(\mathbf{x}_S, t)$ in eq. (11) which shapes the different autocorrelations of the different sources to an average autocorrelation function $S(t)$; in eq. (28) this filter is not needed.

$\Gamma(\mathbf{x}, \mathbf{x}_A, t)$ as defined in eq. (29) is the crosscorrelation of the inward-propagating wavefields at $\mathbf{x}$ and $\mathbf{x}_A$, summed over the sources (van der Neut *et al.* 2010), see Fig. 3(c). We call $\Gamma(\mathbf{x}, \mathbf{x}_A, t)$ the interferometric point-spread function (or plainly the point-spread function). If we would have a regular distribution of sources with equal autocorrelation functions $S(t)$ along a large planar source boundary, and if the medium between the source and receiver boundaries were homogeneous and lossless, the point-spread function would approach a temporally and spatially band-limited delta function, see Appendix for details. Hence, for this situation eq. (27) merely states that the correlation function $C(\mathbf{x}_B, \mathbf{x}_A, t)$ is proportional to the response of a temporally and spatially band-limited source. In practice, there are many factors that make the point-spread function $\Gamma(\mathbf{x}, \mathbf{x}_A, t)$ deviate from a band-limited delta function. Among these factors are simultaneous source acquisition (Section 4.5), medium inhomogeneities (Section 5.1), multiple reflections in the illuminating wavefield (Section 5.2), intrinsic losses (Section 5.3), irregularity of the source distribution (Sections 6.1 and 6.2), etc. For all those cases eq. (27) shows that the point-spread

function blurs the source of the Green's function in the spatial directions and generates ghosts ('spurious multiples', Snieder *et al.* (2006b)) in the temporal direction. MDD involves inverting eq. (27), see Section 4.6. Ideally, this removes the distorting effects of the point-spread function $\Gamma(\mathbf{x}, \mathbf{x}_A, t)$ from the correlation function $C(\mathbf{x}_B, \mathbf{x}_A, t)$ and yields an improved estimate of the Green's function $\bar{G}_{\rm d}(\mathbf{x}_B, \mathbf{x}, t)$.

Note that the interferometric point-spread function $\Gamma(\mathbf{x}, \mathbf{x}_A, t)$ plays a similar role in interferometry by MDD as the point-spread function (or spatial resolution function) in optical, acoustical and seismic imaging systems (Born & Wolf 1965; Norton 1992; Miller *et al.* 1987; Schuster & Hu 2000; Gelius *et al.* 2002; Lecomte 2008; Toxopeus *et al.* 2008; van Veldhuizen *et al.* 2008). For example, in seismic migration the point-spread function is defined as the migration result of the response of a single point scatterer. It is a useful tool to assess migration results in relation with geological parameters, background model, acquisition parameters, etc. Moreover, it is sometimes used in migration deconvolution to improve the spatial resolution of the migration image (Hu *et al.* 2001; Yu *et al.* 2006). In a similar way, van der Neut & Thorbecke (2009) use the interferometric point-spread function $\Gamma(\mathbf{x}, \mathbf{x}_A, t)$ to assess the quality of the virtual source obtained by correlation-based interferometry. Moreover, analogous to migration deconvolution, interferometry by MDD [i.e. inversion of eq. (27)] aims at deblurring and deghosting the virtual source. An important difference is that the interferometric point-spread function is obtained from measured responses, whereas the point-spread function used in migration deconvolution is modelled in a background medium. As a result, the interferometric point-spread function accounts much more accurately for the distorting effects of the medium inhomogeneities, including multiple scattering.

4.4 Noise sources

We show that eq. (27) also holds for the situation of simultaneously acting uncorrelated noise sources. To this end, we define the correlation function and the point-spread function, respectively, as

$$C(\mathbf{x}_B, \mathbf{x}_A, t) = \langle u(\mathbf{x}_B, t) * u^{\rm in}(\mathbf{x}_A, -t) \rangle \,, \tag{31}$$

$$\Gamma(\mathbf{x}, \mathbf{x}_A, t) = \langle u^{\rm in}(\mathbf{x}, t) * u^{\rm in}(\mathbf{x}_A, -t) \rangle \,, \tag{32}$$

where the noise responses are defined as

$$u^{\rm in}(\mathbf{x}_A, t) = \sum_i G^{\rm in}\left(\mathbf{x}_A, \mathbf{x}_S^{(i)}, t\right) * N^{(i)}(t), \tag{33}$$

$$u^{\rm in}(\mathbf{x}, t) = \sum_j G^{\rm in}\left(\mathbf{x}, \mathbf{x}_S^{(j)}, t\right) * N^{(j)}(t), \tag{34}$$

$$u(\mathbf{x}_B, t) = \sum_j G\left(\mathbf{x}_B, \mathbf{x}_S^{(j)}, t\right) * N^{(j)}(t), \tag{35}$$

in which the noise signals are assumed to be mutually uncorrelated, according to

$$\langle N^{(j)}(t) * N^{(i)}(-t) \rangle = \delta_{ij} S^{(i)}(t). \tag{36}$$

Upon substitution of eqs (33)−(35) into eqs (31) and (32), using eq. (36), it follows that the correlation function and the point-spread function as defined in eqs (31) and (32) are identical to those defined in eqs (28) and (29). Hence, whether we consider transient or noise sources, eq. (27) is the relation that needs to be inverted by MDD to resolve the Green's function $\bar{G}_{\rm d}(\mathbf{x}_B, \mathbf{x}, t)$.

Note that the correlation function $C(\mathbf{x}_B, \mathbf{x}_A, t)$ as defined in eq. (31) resembles that defined in eq. (17). There are again three main differences. Eq. (17) is the correlation of noise responses which are defined as integrals over sources on $\mathbb{S}_{\rm src}$ (eqs 14 and 15), whereas the correlated responses in eq. (31) are defined as summations over individual sources (eqs 33 and 35). As mentioned before, this reflects the difference in assumptions on the regularity of the source distribution (see Sections 6.1 and 6.2). Furthermore, in eq. (17) the full noise fields at $\mathbf{x}_A$ and $\mathbf{x}_B$ are crosscorrelated, whereas in eq. (31) the inward-propagating part of the noise field at $\mathbf{x}_A$ is crosscorrelated with the full (or outward-propagating) noise field at $\mathbf{x}_B$. Finally, an underlying assumption of eq. (17) is that the noise sources all have the same autocorrelation function $S(t)$ (eq. 16), whereas eq. (31) is still valid when the autocorrelations of the different sources are different from one another (eq. 36).

4.5 Simultaneous source acquisition

A new trend in the seismic exploration community is simultaneous source acquisition, also known as blended acquisition (Beasley *et al.* 1998; Bagaini 2006; Ikelle 2007; Stefani *et al.* 2007; Howe *et al.* 2008; Hampson *et al.* 2008; Berkhout 2008). Seismic sources are fired with relatively small intervals one after the other, to reduce the total acquisition time. As a result, the seismic response can be seen as a superposition of time-delayed seismic shot records. Using standard shot-record oriented processing and imaging, 'crosstalk' between the sources causes the images to be noisy. The crosstalk can be reduced by using phase-encoded sources (Bagaini 2006; Ikelle 2007) or simultaneous noise sources (Howe *et al.* 2008), by randomizing the time interval between the shots (Stefani *et al.* 2007; Hampson *et al.* 2008), or by inverting the 'blending operator' (Berkhout 2008). Here, we briefly discuss deblending as a form of seismic interferometry by MDD.

Consider the configuration depicted in Fig. 4, where $\boldsymbol{\sigma}^{(m)}$ denotes a group of source positions $\mathbf{x}_S^{(i)}$. Although the figure suggests that these sources are adjacent to each other, they may also be randomly selected from the total array of sources. Assuming the source at $\mathbf{x}_S^{(i)}$ emits a

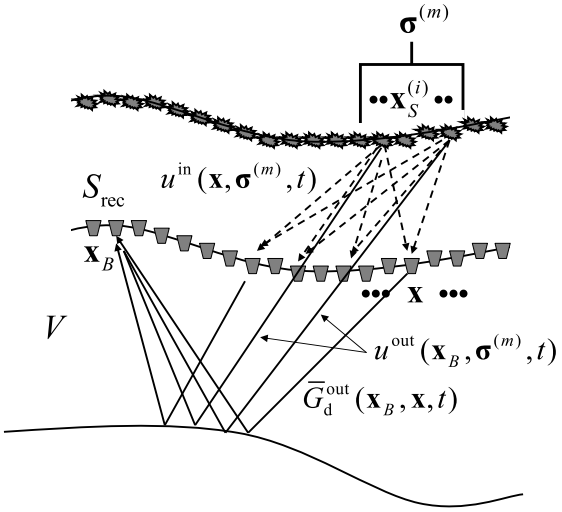

Figure 4. Convolutional model underlying deblending by MDD.

delayed source wavelet $s^{(i)}(t-t_i)$, the blended inward- and outward-propagating fields at $\mathbb{S}_{\mathrm{rec}}$ are given by

$$u^{\mathrm{in}}(\mathbf{x},\boldsymbol{\sigma}^{(m)},t)=\sum_{\mathbf{x}_S^{(i)}\in\boldsymbol{\sigma}^{(m)}} G^{\mathrm{in}}\left(\mathbf{x},\mathbf{x}_S^{(i)},t\right)*s^{(i)}(t-t_i), \tag{37}$$

$$u^{\mathrm{out}}(\mathbf{x}_B,\boldsymbol{\sigma}^{(m)},t)=\sum_{\mathbf{x}_S^{(i)}\in\boldsymbol{\sigma}^{(m)}} G^{\mathrm{out}}\left(\mathbf{x}_B,\mathbf{x}_S^{(i)},t\right)*s^{(i)}(t-t_i), \tag{38}$$

where $\mathbf{x}_S^{(i)}\in\boldsymbol{\sigma}^{(m)}$ denotes that the summation takes place over all source positions $\mathbf{x}_S^{(i)}$ in group $\boldsymbol{\sigma}^{(m)}$. By convolving both sides of eq. (23) with $s^{(i)}(t-t_i)$ and summing over all sources in $\boldsymbol{\sigma}^{(m)}$ we obtain, analogous to eq. (26),

$$u^{\mathrm{out}}(\mathbf{x}_B,\boldsymbol{\sigma}^{(m)},t)=\int_{\mathbb{S}_{\mathrm{rec}}}\bar{G}_{\mathrm{d}}^{\mathrm{out}}(\mathbf{x}_B,\mathbf{x},t)*u^{\mathrm{in}}(\mathbf{x},\boldsymbol{\sigma}^{(m)},t)\,\mathrm{d}\mathbf{x}. \tag{39}$$

When the receivers on $\mathbb{S}_{\mathrm{rec}}$ are real receivers in a borehole, then $u^{\mathrm{out}}(\mathbf{x}_B,\boldsymbol{\sigma}^{(m)},t)$ and $u^{\mathrm{in}}(\mathbf{x},\boldsymbol{\sigma}^{(m)},t)$ are (decomposed) measured blended wavefields in the borehole. On the other hand, in case of surface data acquisition, $u^{\mathrm{out}}(\mathbf{x}_B,\boldsymbol{\sigma}^{(m)},t)$ represents the blended data after model-based receiver redatuming to $\mathbb{S}_{\mathrm{rec}}$ and $u^{\mathrm{in}}(\mathbf{x},\boldsymbol{\sigma}^{(m)},t)$ represents the blended sources, forward extrapolated through the model to $\mathbb{S}_{\mathrm{rec}}$.

Analogous to Section 4.3 we obtain the normal equation by crosscorrelating both sides of eq. (39) with $u^{\mathrm{in}}(\mathbf{x}_A,\boldsymbol{\sigma}^{(m)},t)$ (with $\mathbf{x}_A$ on $\mathbb{S}_{\mathrm{rec}}$) and taking the sum over all source groups $\boldsymbol{\sigma}^{(m)}$. This gives

$$C(\mathbf{x}_B,\mathbf{x}_A,t)=\int_{\mathbb{S}_{\mathrm{rec}}}\bar{G}_{\mathrm{d}}^{\mathrm{out}}(\mathbf{x}_B,\mathbf{x},t)*\Gamma(\mathbf{x},\mathbf{x}_A,t)\,\mathrm{d}\mathbf{x}, \tag{40}$$

where

$$C(\mathbf{x}_B,\mathbf{x}_A,t)=\sum_m u^{\mathrm{out}}\left(\mathbf{x}_B,\boldsymbol{\sigma}^{(m)},t\right)*u^{\mathrm{in}}\left(\mathbf{x}_A,\boldsymbol{\sigma}^{(m)},-t\right), \tag{41}$$

$$\Gamma(\mathbf{x},\mathbf{x}_A,t)=\sum_m u^{\mathrm{in}}\left(\mathbf{x},\boldsymbol{\sigma}^{(m)},t\right)*u^{\mathrm{in}}\left(\mathbf{x}_A,\boldsymbol{\sigma}^{(m)},-t\right). \tag{42}$$

The correlation function defined in eq. (41) is similar to that in eq. (28), except that it is contaminated by crosstalk between the sources within each source group $\boldsymbol{\sigma}^{(m)}$. The point-spread function defined in eq. (42) also contains crosstalk contributions. In Section 5.1, we present some examples of this point-spread function. Deblending involves inverting eq. (40) by MDD. Ideally this eliminates the crosstalk from the correlation function and gives the deblended virtual source response $\bar{G}_{\mathrm{d}}^{\mathrm{out}}(\mathbf{x}_B,\mathbf{x},t)$.

The discussed representations for blended data have two interesting limiting cases. When each source group $\boldsymbol{\sigma}^{(m)}$ consists of a single source, then we obtain the expressions for transient sources discussed in Sections 4.2 and 4.3. On the other hand, when there is only one source group containing all sources and when the source wavelets are replaced by mutually uncorrelated noise signals, then we obtain the expressions for noise sources discussed in Section 4.4.

4.6 Resolving the Green's function

Interferometry by MDD essentially involves inversion of eq. (27) (or 40). In general, the existence of the inverse of the point-spread function is not guaranteed. Recall from eqs (29), (32) and (42) that the point-spread function (explicitly or implicitly) involves a summation over source positions. To evaluate this function, the source positions do not need to be known and the source distribution does not need to be regular, but

clearly the well-posedness of its inverse depends on the number of available sources, the total source aperture and the source bandwidth. In practical situations a spectral analysis of the point-spread function helps to assess for which spatial and temporal frequencies the inversion can be carried out (van der Neut *et al.* 2011).

For the actual inversion of eq. (27) (or 40) we transform this equation to the frequency domain and replace the integration along the receivers by a summation, according to

$$\hat{C}\left(\mathbf{x}_B, \mathbf{x}_A^{(l)}, \omega\right) = \sum_k \hat{\bar{G}}_{\mathrm{d}}(\mathbf{x}_B, \mathbf{x}^{(k)}, \omega)\hat{\Gamma}\left(\mathbf{x}^{(k)}, \mathbf{x}_A^{(l)}, \omega\right), \tag{43}$$

for all $\mathbf{x}_A^{(l)}$ on the receiver surface $\mathbb{S}_{\mathrm{rec}}$. Note that this discretization assumes a regular sampling of the receiver coordinate $\mathbf{x}^{(k)}$. This is a less severe restriction than that for discretizing a source integral [like the one in eq. (11)], because the receivers are often well sampled and their positions are usually known. In case of irregular receiver sampling, a regularization procedure (Duijndam *et al.* 1999) could be applied prior to inverting eq. (43). The system of eq. (43) can be solved for $\hat{\bar{G}}_{\mathrm{d}}(\mathbf{x}_B, \mathbf{x}^{(k)}, \omega)$ for each frequency component separately. In practice this is done by a stabilized matrix inversion per frequency component, while taking care of the limitations discussed above. Transforming the end-result back to the time domain gives a band-limited estimate of $\bar{G}_{\mathrm{d}}(\mathbf{x}_B, \mathbf{x}^{(k)}, t)$, which completes the MDD process.

It is beyond the scope of this paper to discuss the numerical aspects of the matrix inversion. The inversion is similar to that proposed by Berkhout (1982) and Wapenaar & Berkhout (1989) in the context of model-based inverse seismic wavefield extrapolation and imaging. Tanter *et al.* (2000) apply matrix inversion to a measured wavefield propagator in the context of the time-reversal method and thus improve the source imaging capabilities of that method. Whereas Berkhout (1982) proposes least-squares inversion, Tanter *et al.* (2000) employ singular-value decomposition to invert the matrix. Similarly, in seismic interferometry by MDD the matrix inversion can be done by least-squares inversion (Wapenaar *et al.* 2008b) or by singular-value decomposition (Minato *et al.* 2011). We refer to van der Neut *et al.* (2011) for a discussion on the stability aspects of interferometry by MDD, and to Ruigrok *et al.* (2010) and Hunziker *et al.* (2010) for a discussion on the sampling and illumination aspects.

4.7 Vectorial fields

Until now we considered scalar fields. For vectorial fields the representations and algorithms are straightforward extensions of those discussed above. Here, we discuss the main modifications. The convolutional representation (26) is for vectorial fields extended to

$$\mathbf{u}(\mathbf{x}_B, \mathbf{x}_S^{(i)}, t) = \int_{\mathbb{S}_{\mathrm{rec}}} \bar{\mathbf{G}}_{\mathrm{d}}(\mathbf{x}_B, \mathbf{x}, t) * \mathbf{u}^{\mathrm{in}}\left(\mathbf{x}, \mathbf{x}_S^{(i)}, t\right) \mathrm{d}\mathbf{x} \tag{44}$$

(the integrand is a convolutional matrix–vector product). Here $\mathbf{u}^{\mathrm{in}}(\mathbf{x}, \mathbf{x}_S^{(i)}, t)$ and $\mathbf{u}(\mathbf{x}_B, \mathbf{x}_S^{(i)}, t)$ are the inward propagating and total (or outward-propagating) field vectors, respectively, due to transient sources at $\mathbf{x}_S^{(i)}$ (in the case of simultaneous source acquisition, the source positions $\mathbf{x}_S^{(i)}$ need to be replaced by source groups $\boldsymbol{\sigma}^{(m)}$). For example, for the situation of elastodynamic waves the field vectors are defined as

$$\mathbf{u}^{\mathrm{in}} = \begin{pmatrix} \Phi^{\mathrm{in}} \\ \Psi^{\mathrm{in}} \\ \Upsilon^{\mathrm{in}} \end{pmatrix} \quad \text{and} \quad \mathbf{u} = \begin{pmatrix} \Phi \\ \Psi \\ \Upsilon \end{pmatrix}, \tag{45}$$

where Φ, Ψ and Υ represent P, S_1 and S_2 waves, respectively. In practice these fields are obtained by applying decomposition of multicomponent data. Moreover, for this situation, $\bar{\mathbf{G}}_{\mathrm{d}}(\mathbf{x}_B, \mathbf{x}, t)$ can be written as

$$\bar{\mathbf{G}}_{\mathrm{d}}(\mathbf{x}_B, \mathbf{x}, t) = \begin{pmatrix} \bar{G}_{\mathrm{d}}^{\phi,\phi} & \bar{G}_{\mathrm{d}}^{\phi,\psi} & \bar{G}_{\mathrm{d}}^{\phi,\upsilon} \\ \bar{G}_{\mathrm{d}}^{\psi,\phi} & \bar{G}_{\mathrm{d}}^{\psi,\psi} & \bar{G}_{\mathrm{d}}^{\psi,\upsilon} \\ \bar{G}_{\mathrm{d}}^{\upsilon,\phi} & \bar{G}_{\mathrm{d}}^{\upsilon,\psi} & \bar{G}_{\mathrm{d}}^{\upsilon,\upsilon} \end{pmatrix} (\mathbf{x}_B, \mathbf{x}, t), \tag{46}$$

where the Green's function $\bar{G}_{\mathrm{d}}^{p,q}(\mathbf{x}_B, \mathbf{x}, t)$ is the dipole response [analogous to eq. (20)] of the medium in $\mathbb{V}$ (with absorbing boundary conditions at $\mathbb{S}_{\mathrm{rec}}$) in terms of an inward-propagating q-type wavefield at source position $\mathbf{x}$ and a total (or outward-propagating) p-type wavefield at receiver position $\mathbf{x}_B$ (Wapenaar & Berkhout 1989). When the sources at $\mathbf{x}_S^{(i)}$ are multicomponent sources, eq. (44) can be extended to

$$\mathbf{U}\left(\mathbf{x}_B, \mathbf{x}_S^{(i)}, t\right) = \int_{\mathbb{S}_{\mathrm{rec}}} \bar{\mathbf{G}}_{\mathrm{d}}(\mathbf{x}_B, \mathbf{x}, t) * \mathbf{U}^{\mathrm{in}}\left(\mathbf{x}, \mathbf{x}_S^{(i)}, t\right) \mathrm{d}\mathbf{x}, \tag{47}$$

where $\mathbf{U}^{\mathrm{in}}$ and $\mathbf{U}$ are matrices of which the columns contain field vectors $\mathbf{u}^{\mathrm{in}}$ and $\mathbf{u}$ for different source components (similar as the different columns of $\bar{\mathbf{G}}_{\mathrm{d}}$ are related to different source types). Eqs (44) and (47) are not restricted to the elastodynamic situation but apply to any vectorial wave or diffusion field, including electromagnetic, poroelastic and seismoelectric fields (Wapenaar *et al.* 2008a).

Interferometry by MDD means that eq. (47) needs to be solved for $\bar{\mathbf{G}}_{\mathrm{d}}(\mathbf{x}_B, \mathbf{x}, t)$. Similar as for the scalar situation, the well-posedness of this inverse problem depends on the number of available sources, the source aperture, the bandwidth and, in addition, the number of independent source components. Since the Green's matrix is resolved by MDD, the sources do not need to be regularly distributed and the source components do not need to be mutually orthonormal.

Similar as in the scalar case, to obtain the normal equation for least-squares inversion, we crosscorrelate both sides of eq. (47) with the transposed of $\mathbf{U}^{\text{in}}(\mathbf{x}_A, \mathbf{x}_S^{(i)}, t)$ (with $\mathbf{x}_A$ on $\mathbb{S}_{\text{rec}}$) and take the sum over all sources, according to

$$\mathbf{C}(\mathbf{x}_B, \mathbf{x}_A, t) = \int_{\mathbb{S}_{\text{rec}}} \bar{\mathbf{G}}_{\text{d}}(\mathbf{x}_B, \mathbf{x}, t) * \mathbf{\Gamma}(\mathbf{x}, \mathbf{x}_A, t)\, \text{d}\mathbf{x}, \tag{48}$$

where

$$\mathbf{C}(\mathbf{x}_B, \mathbf{x}_A, t) = \sum_i \mathbf{U}\left(\mathbf{x}_B, \mathbf{x}_S^{(i)}, t\right) * \left\{\mathbf{U}^{\text{in}}\left(\mathbf{x}_A, \mathbf{x}_S^{(i)}, -t\right)\right\}^t, \tag{49}$$

$$\mathbf{\Gamma}(\mathbf{x}, \mathbf{x}_A, t) = \sum_i \mathbf{U}^{\text{in}}\left(\mathbf{x}, \mathbf{x}_S^{(i)}, t\right) * \left\{\mathbf{U}^{\text{in}}\left(\mathbf{x}_A, \mathbf{x}_S^{(i)}, -t\right)\right\}^t, \tag{50}$$

with superscript ^{t} denoting transposition. Here $\mathbf{C}(\mathbf{x}_B, \mathbf{x}_A, t)$ and $\mathbf{\Gamma}(\mathbf{x}, \mathbf{x}_A, t)$ are the correlation and point-spread functions, respectively, in matrix form. Eq. (48) shows again that the correlation function is proportional to the sought Green's function $\bar{\mathbf{G}}_{\text{d}}(\mathbf{x}_B, \mathbf{x}, t)$ with its source smeared in space and time by the point-spread function.

For the situation of noise sources the correlation and point-spread matrices are given by

$$\mathbf{C}(\mathbf{x}_B, \mathbf{x}_A, t) = \left\langle \mathbf{u}(\mathbf{x}_B, t) * \{\mathbf{u}^{\text{in}}(\mathbf{x}_A, -t)\}^t \right\rangle, \tag{51}$$

$$\mathbf{\Gamma}(\mathbf{x}, \mathbf{x}_A, t) = \left\langle \mathbf{u}^{\text{in}}(\mathbf{x}, t) * \{\mathbf{u}^{\text{in}}(\mathbf{x}_A, -t)\}^t \right\rangle, \tag{52}$$

where, analogous to eqs (33)−(35), the field vectors $\mathbf{u}^{\text{in}}$ and $\mathbf{u}$ are the responses of simultaneously acting mutually uncorrelated multicomponent noise sources. It can be shown in a similar way as in Section 4.4 that the correlation and point-spread functions defined in eqs (51) and (52) are identical to those defined in (49) and (50). Hence, whether we consider transient or noise sources, eq. (48) is the relation that needs to be inverted by MDD to resolve the Green's function $\bar{\mathbf{G}}_{\text{d}}(\mathbf{x}_B, \mathbf{x}, t)$. This is done in a similar way as described in Section 4.6 for the scalar situation.

5 APPLICATIONS IN CONTROLLED-SOURCE INTERFEROMETRY

Unlike ambient-noise interferometry, controlled-source interferometry is usually applied to situations in which the sources are regularly distributed along a surface (Schuster 2009). Hence, for controlled-source interferometry, MDD is usually not required to correct for an irregular source distribution. However, there are several other limiting factors in controlled-source interferometry for which MDD may provide a solution. In the following sections, we show with numerical examples how MDD accounts for the effects of medium inhomogeneities in the 'virtual source method' (Section 5.1), for multiples in the illuminating wavefield in ocean-bottom multiple elimination (Section 5.2) and for losses in CSEM interferometry (Section 5.3).

5.1 'Virtual source method'

Although creating a virtual source is the essence of all seismic interferometry methods, in the seismic exploration literature the term 'virtual source method' is often synonymous with the method developed by Bakulin & Calvert (2004, 2006). Fig. 2(b) shows the basic configuration. Sources are present at the Earth's surface, denoted by $\mathbb{S}_{\text{src}}$. The responses of these sources are measured in a near-horizontal borehole, below a complex overburden. The responses $u(\mathbf{x}_A, \mathbf{x}_S, t)$ and $u(\mathbf{x}_B, \mathbf{x}_S, t)$ at any combination of two receivers $\mathbf{x}_A$ and $\mathbf{x}_B$ in the borehole are crosscorrelated and the results are integrated along the sources $\mathbf{x}_S$ at $\mathbb{S}_{\text{src}}$, according to eq. (11). The correlation function $C(\mathbf{x}_B, \mathbf{x}_A, t)$ is interpreted as the response at $\mathbf{x}_B$ of a virtual source at $\mathbf{x}_A$. Because this virtual source is situated below the complex overburden, its response contains less-distorted reflections of the deeper target than the original responses of the sources at the surface $\mathbb{S}_{\text{src}}$.

From the theory it follows that this method involves approximations. If $\mathbb{S}_{\text{src}}$ were a closed surface, the correlation function $C(\mathbf{x}_B, \mathbf{x}_A, t)$ would be proportional to $\{G(\mathbf{x}_B, \mathbf{x}_A, t) + G(\mathbf{x}_B, \mathbf{x}_A, -t)\} * S(t)$ (eq. 13), in which $G(\mathbf{x}_B, \mathbf{x}_A, t) * S(t)$ is indeed the response of a virtual source at $\mathbf{x}_A$. However, because $\mathbb{S}_{\text{src}}$ is limited to a part of the Earth's surface, the correlation function is a distorted version of $G(\mathbf{x}_B, \mathbf{x}_A, t) * S(t)$ and contains spurious multiples (Snieder *et al.* 2006b). To compensate for this, Bakulin & Calvert (2004) apply a time window around the first arrival of $u(\mathbf{x}_A, \mathbf{x}_S, t)$. Bakulin & Calvert (2006) propose to replace the correlation by a trace-by-trace deconvolution for the downgoing part of $u(\mathbf{x}_A, \mathbf{x}_S, t)$. They show that this approach compensates for variations in the source wavelet and, partly, for reverberations in the overburden. The spurious multiples can be further suppressed by applying up/down decomposition to $u(\mathbf{x}_B, \mathbf{x}_S, t)$ as well as $u(\mathbf{x}_A, \mathbf{x}_S, t)$ (Mehta *et al.* 2007a; van der Neut & Wapenaar 2009).

We illustrate the correlation approach with a numerical example. Fig. 5(a) shows the configuration, with a regular distribution of sources at the surface (denoted by the black dots) and receivers in a horizontal borehole (the green triangles at $x_3 = 500$ m). The upper part of the overburden, that is, the medium between the sources and the receivers, contains significant variations of the medium parameters in the lateral as well as in the vertical direction. Below the receivers there is a reservoir layer (the orange layer in Fig. 5a). The lower part of the overburden, that is, the medium between the receivers in the borehole and the reservoir, is homogeneous (the light-green layer). Fig. 5(b) shows a modelled response of a source at the centre of the surface, observed by the receivers in the borehole. The modelling was done without free-surface effects. The response of the reservoir is denoted by the arrow. It is distorted by the inhomogeneities of the overburden. The aim of the 'virtual

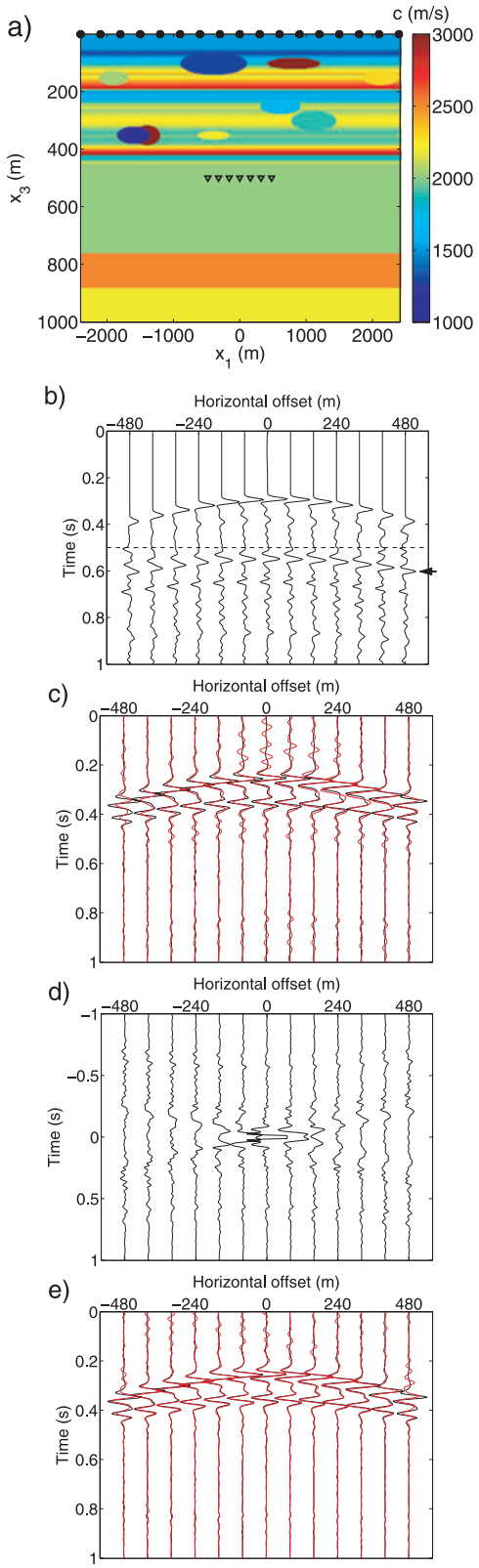

Figure 5. (a) Configuration for the 'virtual source method'. The sources are situated at the surface (black dots) and the receivers in a horizontal borehole (the green triangles at $x_3 = 500$ m) below a complex overburden. (b) Modelled response of a source at the centre of the surface. The amplitudes below the dashed line have been multiplied by a factor 3. (c) Result of interferometry by crosscorrelation of decomposed wavefields (red), compared with directly modelled reflection response of a source at the centre of the borehole (black). (d) Point-spread function (clipped at 20 per cent of its maximum amplitude). (e) MDD result (red) compared with modelled response (black).

source method' is to reduce these distortions. We follow the approach of Mehta *et al.* (2007a), hence, we first apply decomposition of the field observed in the borehole into downgoing and upgoing waves. This requires that multicomponent data are available (in this case the acoustic pressure and the normal particle velocity component). We call the decomposed fields $u^{\rm in}(\mathbf{x}_A, \mathbf{x}_S^{(i)}, t)$ and $u^{\rm out}(\mathbf{x}_B, \mathbf{x}_S^{(i)}, t)$, respectively. The correlation function is defined, analogous to eq. (28), as

$$C(\mathbf{x}_B, \mathbf{x}_A, t) = \sum_i u^{\rm out}\left(\mathbf{x}_B, \mathbf{x}_S^{(i)}, t\right) * u^{\rm in}\left(\mathbf{x}_A, \mathbf{x}_S^{(i)}, -t\right). \tag{53}$$

The virtual source at $\mathbf{x}_A$ is chosen at the centre of the borehole whereas the receiver coordinate $\mathbf{x}_B$ varies along the borehole. Fig. 5(c) shows this correlation function in red. The directly modelled reflection response of a source for downgoing waves at $\mathbf{x}_A$ is shown in black in this same figure. Note that the retrieved reservoir response matches the modelled response reasonably well, but still we observe some distortions along this reflection event as well as some spurious events at later times.

Interferometry by MDD provides a more accurate way to retrieve the virtual source response. Fig. 3(b) shows the configuration. Assuming a regular source distribution, this configuration corresponds to that of Fig. 2(b), except that Fig. 3(b) illustrates the convolutional representation that underlies MDD. The response $u^{\rm out}(\mathbf{x}_B, \mathbf{x}_S^{(i)}, t)$ is defined, analogous to eq. (26), as

$$u^{\rm out}\left(\mathbf{x}_B, \mathbf{x}_S^{(i)}, t\right) = \int_{\mathbb{S}_{\rm rec}} \bar{G}_{\rm d}^{\rm out}(\mathbf{x}_B, \mathbf{x}, t) * u^{\rm in}\left(\mathbf{x}, \mathbf{x}_S^{(i)}, t\right) \,{\rm d}\mathbf{x}, \tag{54}$$

that is, the convolution of the inward propagating wavefield $u^{\rm in}(\mathbf{x}, \mathbf{x}_S^{(i)}, t)$ with the Green's function $\bar{G}_{\rm d}^{\rm out}(\mathbf{x}_B, \mathbf{x}, t)$, integrated along the receivers $\mathbf{x}$ in the borehole. This borehole is denoted as $\mathbb{S}_{\rm rec}$. Our aim is to retrieve $\bar{G}_{\rm d}^{\rm out}(\mathbf{x}_B, \mathbf{x}, t)$ by inverting, analogous to eq. (27), the normal equation

$$C(\mathbf{x}_B, \mathbf{x}_A, t) = \int_{\mathbb{S}_{\rm rec}} \bar{G}_{\rm d}^{\rm out}(\mathbf{x}_B, \mathbf{x}, t) * \Gamma(\mathbf{x}, \mathbf{x}_A, t) \,{\rm d}\mathbf{x}. \tag{55}$$

The correlation function $C(\mathbf{x}_B, \mathbf{x}_A, t)$ at the left-hand side was already shown in Fig. 5(c). The point-spread function $\Gamma(\mathbf{x}, \mathbf{x}_A, t)$ at the right-hand side is obtained, according to eq. (29), by crosscorrelating $u^{\rm in}(\mathbf{x}, \mathbf{x}_S^{(i)}, t)$ with $u^{\rm in}(\mathbf{x}_A, \mathbf{x}_S^{(i)}, t)$ and summing over the sources. It is shown in Fig. 5(d) for fixed $\mathbf{x}_A$ and variable $\mathbf{x}$. Note that it deviates significantly from the band-limited delta function in Fig. A1, due to the inhomogeneities of the overburden. According to eq. (55) this point-spread function smears the source of $\bar{G}_{\rm d}^{\rm out}(\mathbf{x}_B, \mathbf{x}, t)$ in space and time, which explains the distortions along the reflection event in Fig. 5(c). By applying MDD, that is, deconvolving the correlation function in Fig. 5(c) for the point-spread function of Fig. 5(d), we obtain an estimate of the Green's function $\bar{G}_{\rm d}^{\rm out}(\mathbf{x}_B, \mathbf{x}, t)$. The result (for $\mathbf{x} = \mathbf{x}_A$ fixed at the central geophone and variable $\mathbf{x}_B$) is shown in Fig. 5(e) by the red traces (for display purposes convolved with $S(t)$), where it is compared with the directly modelled response (black traces). Note that the match is nearly perfect and that the spurious events vanished, which confirms that in this example MDD properly corrects for the inhomogeneities of the overburden.

The elastodynamic extension of this approach yields improved virtual *P*- and *S*-wave source responses with reliable amplitudes along the reflection events (van der Neut *et al.* 2011), suited for quantitative amplitude-versus-angle inversion. A further discussion is beyond the scope of this paper.

We conclude this section by presenting the point-spread function for the situation of simultaneous source acquisition. We consider a similar configuration as in Fig. 5(a), except that for simplicity the propagation velocity is taken constant at 2000 m s^{-1}. There are 256 sources at the surface with a lateral spacing of 20 m. We form 64 source groups $\boldsymbol{\sigma}^{(m)}$, each containing four adjacent sources which emit transient wavelets, 0.25 s after one another. The inward-propagating field $u^{\rm in}(\mathbf{x}, \boldsymbol{\sigma}^{(m)}, t)$ at the receiver array at $x_3 = 500$ m is defined by eq. (37). The point-spread function $\Gamma(\mathbf{x}, \mathbf{x}_A, t)$, as defined in eq. (42), is shown in Fig. 6(a), with $\mathbf{x}_A$ fixed at the centre of the array and $\mathbf{x}$ variable along the array. Note that the band-limited delta function around $\mathbf{x} = \mathbf{x}_A$ and $t = 0$ in Fig. 6(a) resembles that in Fig. A1, because the medium is homogeneous in both cases. However, Fig. 6(a) contains in addition a number of temporally and spatially shifted band-limited delta functions, as a result of the crosstalk between the sources within each source group $\boldsymbol{\sigma}^{(m)}$. These shifted delta functions explain the crosstalk in the correlation function $C(\mathbf{x}_B, \mathbf{x}_A, t)$ via eq. (40). To obtain the deblended virtual source response $\bar{G}_{\rm d}^{\rm out}(\mathbf{x}_B, \mathbf{x}, t)$ from $C(\mathbf{x}_B, \mathbf{x}_A, t)$, eq. (40) needs to be inverted (not shown).

As mentioned in Section 4.5, the crosstalk associated to standard shot-record oriented processing of blended data is sometimes reduced by randomizing the time interval between the shots. We add random variations (uniform between +50 per cent and −50 per cent) to the 0.25 s time interval and evaluate again the point-spread function $\Gamma(\mathbf{x}, \mathbf{x}_A, t)$, see Fig. 6(b). Note that the band-limited delta function around $\mathbf{x} = \mathbf{x}_A$ and $t = 0$ remains intact, whereas the crosstalk disperses in space and time. Inverting noisy point-spread functions like the one in Fig. 6(b) may be a more stable process than inverting nearly periodic point-spread functions like the one in Fig. 6(a). A further discussion of deblending is beyond the scope of this paper.

5.2 Ocean-bottom multiple elimination

As already mentioned in the introduction, interferometry by MDD is akin to multiple elimination of ocean-bottom data (Amundsen 2001). Here, we briefly review ocean-bottom multiple elimination, explained as an interferometry-by-MDD process. Fig. 7 shows the convolutional model of Fig. 3(b), modified for the situation of ocean-bottom data, including multiple reflections. Eq. (54) gives the relation between the inward- and outward-propagating fields at the ocean bottom and the Green's function $\bar{G}_{\rm d}^{\rm out}(\mathbf{x}_B, \mathbf{x}, t)$. Recall that the bar denotes a reference situation with possibly different boundary conditions at $\mathbb{S}_{\rm rec}$ and/or different medium parameters outside $\mathbb{V}$. For the reference situation we

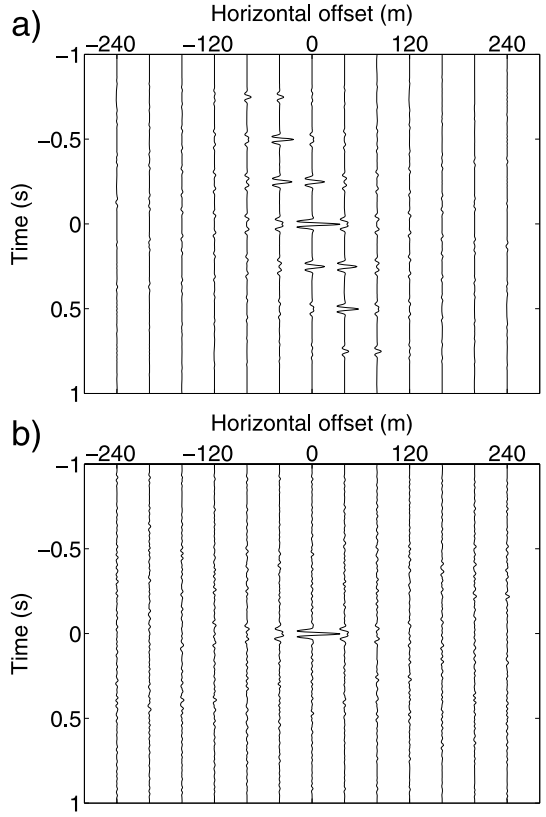

Figure 6. (a) Point-spread function for blended data from 64 groups of four sources each, with a regular time interval of 0.25 s. (b) Idem, after adding random variations to the time interval.

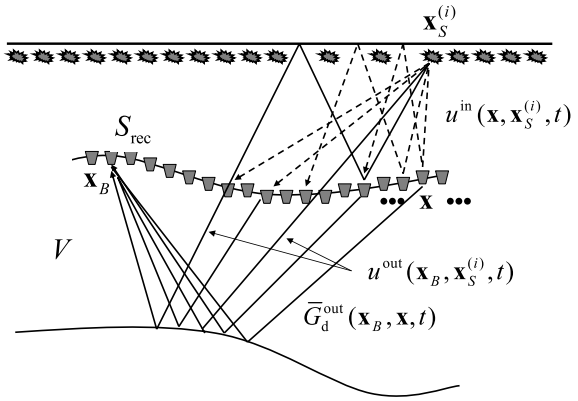

Figure 7. Convolutional model for ocean-bottom data with multiples.

choose an absorbing ocean bottom $\mathbb{S}_{\text{rec}}$ and a homogeneous upper half-space, which implies that $\bar{G}_{\text{d}}^{\text{out}}(\mathbf{x}_B, \mathbf{x}, t)$ is the response of the half-space below $\mathbb{S}_{\text{rec}}$, without any multiple reflections related to the ocean bottom and the water surface. Interferometry by MDD resolves $\bar{G}_{\text{d}}^{\text{out}}(\mathbf{x}_B, \mathbf{x}, t)$ by inverting eq. (55).

We illustrate this with a numerical example. Fig. 8(a) shows the configuration, with sources just below the water surface and multicomponent receivers (acoustic pressure and normal particle velocity) at the ocean bottom. The lower half-space contains a reservoir layer. Fig. 8(b) shows the modelled response of the central source, observed at the ocean bottom. The direct wave and the reservoir response (the latter denoted by an arrow) are clearly distinguishable, as well as many multiple reflections. Decomposition is applied to the multicomponent data at the ocean bottom, using the medium parameters of the first layer below the ocean bottom (Amundsen & Reitan 1995; Schalkwijk *et al.* 2003). This gives the inward and outward-propagating waves $u^{\text{in}}(\mathbf{x}_A, \mathbf{x}_S^{(i)}, t)$ and $u^{\text{out}}(\mathbf{x}_B, \mathbf{x}_S^{(i)}, t)$ just below the ocean bottom. The correlation function, defined in eq. (53), is shown in Fig. 8(c) (red traces), and is compared with the directly modelled response of the reservoir layer (black traces). Note that the match of the correlation function with the reservoir response is quite good, but the correlation function contains in addition many spurious multiple reflections that are not present in the reservoir response. The amplitudes of these spurious multiple reflections, which appear below the horizontal dashed line in Fig. 8(c), have been multiplied by a factor 3 for display purposes (in more complicated situations

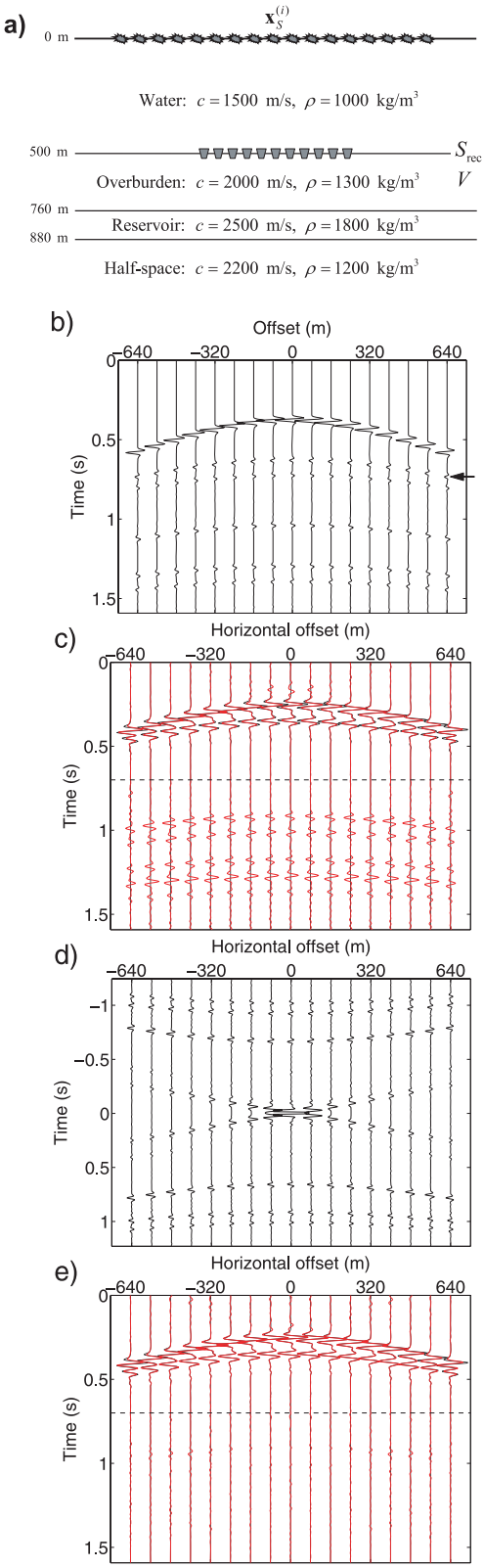

Figure 8. (a) Configuration for ocean-bottom multiple elimination. The sources are situated just below the free surface and the receivers at the ocean bottom. (b) Modelled response of a source at the centre of the surface. (c) Result of interferometry by crosscorrelation of decomposed wavefields (red), compared with directly modelled reflection response of a source at the centre of the ocean bottom (black). The amplitudes below the dashed line have been multiplied by a factor 3. (d) Point-spread function (clipped at 20 per cent of its maximum amplitude). (e) MDD result (red) compared with modelled response (black). The amplitudes below the dashed line have been multiplied by a factor 3.

these spurious multiples would interfere with the retrieved primaries). The point-spread function $\Gamma(\mathbf{x}, \mathbf{x}_A, t)$, defined in eq. (29), is shown in Fig. 8(d). Apart from the band-limited delta function, it contains multiple reflections. According to eq. (55), the correlation function in Fig. 8(c) can be seen as the reservoir response $\bar{G}_{\rm d}^{\rm out}(\mathbf{x}_B, \mathbf{x}, t)$ convolved in space and time with the point-spread function in Fig. 8(d). This explains the spurious multiples in Fig. 8(c). These spurious multiples are removed by deconvolving for the point-spread function, that is, by inverting eq. (55) for $\bar{G}_{\rm d}^{\rm out}(\mathbf{x}_B, \mathbf{x}, t)$. The result of this MDD procedure (for $\mathbf{x} = \mathbf{x}_A$ fixed at the central geophone and variable $\mathbf{x}_B$) is shown in Fig. 8(e) by the red traces (for display purposes convolved with $S(t)$), and is compared with the directly modelled response (black traces). Note that the spurious multiples of Fig. 8(c) have been very well suppressed [for display purposes the amplitudes of the multiple residuals below the dashed line in Fig. 8(e) have been multiplied with the same factor as the spurious multiples in Fig. 8(c)].

We included this example to show the relation between interferometry by MDD and the methodology of ocean-bottom multiple elimination. In the example in Section 5.1, we showed that interferometry by MDD accounts for overburden distortions, but in that example the effect of multiple reflections was small. When borehole data are distorted by overburden effects as well as multiple reflections, interferometry by MDD simultaneously accounts for both types of distortions.

5.3 CSEM interferometry

In controlled-source electromagnetic (CSEM) prospecting, a low-frequency source above the ocean bottom emits a diffusive EM field into the subsurface, of which the response is measured by multicomponent EM receivers at the ocean bottom (Fig. 9a). Although the spatial resolution of CSEM data is much lower than that of seismic data, an important advantage of CSEM prospecting is its potential to detect a hydrocarbon accumulation in a reservoir due to its high conductivity contrast (Ellingsrud *et al.* 2002; Moser *et al.* 2006). Fig. 9(b) shows a modelled 2D CSEM response of an inline electric current source of 0.5 Hz. The source is positioned at the centre of the array, 50 m above the ocean bottom, see Fig. 9(a). This response represents the inline electric field component at the ocean bottom, as a function of source–receiver offset. The receiver sampling is 20 m and the total length of the array is 10 km.

Because a CSEM measurement is nearly monochromatic, the response of a reservoir cannot be separated in time from other events. As a matter of fact, it is largely overshadowed by the direct field and the response of the airwave. Amundsen *et al.* (2006) show that decomposition of CSEM data into downward and upward decaying fields improves the detectability of hydrocarbon reservoirs. Here, we show that the combination of decomposition and interferometry by MDD yields accurate quantitative information about the reservoir response (Slob *et al.* 2007; van den Berg *et al.* 2008).

Decomposition requires that multicomponent data are available. For the example of Fig. 9, this means that apart from the inline electric field data (Fig. 9b), transverse magnetic data are required as well. Using a decomposition algorithm similar as that for seismic data, CSEM data can be decomposed into downward and upward decaying fields (Ursin 1983; Amundsen *et al.* 2006). We designate these fields as $\hat{u}^{\rm in}(\mathbf{x}_A, \mathbf{x}_S^{(i)}, \omega)$ and $\hat{u}^{\rm out}(\mathbf{x}_B, \mathbf{x}_S^{(i)}, \omega)$, respectively, where superscripts 'in' and 'out' denote that at the receiver surface $\mathbb{S}_{\rm rec}$ in Fig. 9(a) these fields diffuse inward to and outward from $\mathbb{V}$, respectively. Note that ω is considered constant ($\omega = 2\pi f$, with $f = 0.5$ Hz).

Because in CSEM we consider monochromatic fields, we replace eqs (29), (53) and (55) by the following frequency-domain expressions

$$\hat{C}(\mathbf{x}_B, \mathbf{x}_A, \omega) = \int_{\mathbb{S}_{\rm rec}} \hat{\bar{G}}_{\rm d}^{\rm out}(\mathbf{x}_B, \mathbf{x}, \omega)\hat{\Gamma}(\mathbf{x}, \mathbf{x}_A, \omega)\, {\rm d}\mathbf{x}, \tag{56}$$

where the correlation function and the point-spread function are defined as

$$\hat{C}(\mathbf{x}_B, \mathbf{x}_A, \omega) = \sum_i \hat{u}^{\rm out}\left(\mathbf{x}_B, \mathbf{x}_S^{(i)}, \omega\right)\left\{\hat{u}^{\rm in}\left(\mathbf{x}_A, \mathbf{x}_S^{(i)}, \omega\right)\right\}^*, \tag{57}$$

$$\hat{\Gamma}(\mathbf{x}, \mathbf{x}_A, \omega) = \sum_i \hat{u}^{\rm in}\left(\mathbf{x}, \mathbf{x}_S^{(i)}, \omega\right)\left\{\hat{u}^{\rm in}\left(\mathbf{x}_A, \mathbf{x}_S^{(i)}, \omega\right)\right\}^*, \tag{58}$$

respectively. $\hat{\bar{G}}_{\rm d}^{\rm out}(\mathbf{x}_B, \mathbf{x}, \omega)$ in eq. (56) is the sought reservoir response that would be obtained with a monochromatic source for an inward diffusing field at $\mathbf{x}$ and a receiver for an outward diffusing field at $\mathbf{x}_B$ (both at $\mathbb{S}_{\rm rec}$), in a configuration with a reflection-free ocean bottom. The monochromatic correlation function defined in eq. (57) is obtained by correlating the inward and outward diffusing fields at $\mathbb{S}_{\rm rec}$. The result is shown in Fig. 9(c) (red curve), where it is compared with the directly modelled response $\hat{\bar{G}}_{\rm d}^{\rm out}(\mathbf{x}_B, \mathbf{x}, \omega)$ (black curve), with $\mathbf{x} = \mathbf{x}_A$ at the centre of the array at $\mathbb{S}_{\rm rec}$. The differences are mainly due to the dissipation of the conducting water layer, for which no compensation takes place in the correlation method. For ease of comparison both responses were normalized so that the maxima of both curves are the same. The deviations at intermediate offsets hinder the quantification of the reservoir parameters.

Fig. 9(d) shows the monochromatic point-spread function, defined in eq. (58). It deviates from a band-limited spatial delta function due to the dissipation of the water layer as well as the interactions with the water surface. MDD involves inversion of eq. (56), that is, removing the effect of the point-spread function of Fig. 9(d) from the correlation function in Fig. 9(c). The result is shown in Fig. 9(e) (red curve), where it perfectly matches the directly modelled result (black curve). Note that, unlike in Fig. 9(c), no normalization was needed here.

This example shows that, at least in principle, interferometry by MDD compensates for dissipation and thus leads to an accurate retrieval of the CSEM reservoir response. The effects of the conducting water layer are completely eliminated, including those of the direct field and the airwave. The final response is independent of the water depth and contains quantitative information about the reservoir layer. It should

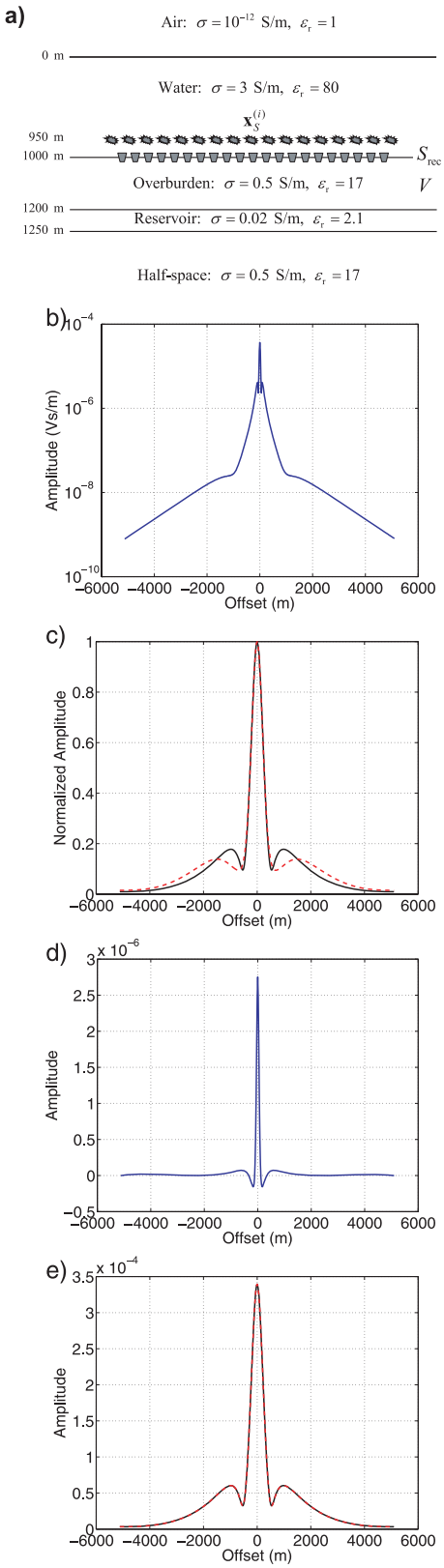

Figure 9. (a) Configuration for CSEM interferometry. The sources just above the ocean bottom are inline electric current sources, emitting monochromatic diffusive EM fields into the subsurface. The receivers at the ocean bottom measure the inline electric field and the transverse magnetic field. (b) Inline electric field at ocean bottom. (c) Result of interferometry by crosscorrelation (red), compared with directly modelled CSEM reservoir response (black). (d) Point-spread function. (e) MDD result (red) compared with modelled response (black).

be noted that we considered an ideal situation of well-sampled data, measured with high precision and no noise added. For a more detailed discussion of CSEM interferometry by MDD, see Hunziker *et al.* (2009, 2010) and Fan *et al.* (2009).

6 APPLICATIONS IN AMBIENT-NOISE INTERFEROMETRY

In ambient-noise interferometry, the sources are unknown and usually irregularly distributed. MDD has the potential to compensate for the source irregularity. We illustrate this aspect with numerical examples for passive surface-wave interferometry (Section 6.1) and for passive body-wave interferometry (Section 6.2).

6.1 Passive surface-wave interferometry

One of the most widely used applications of direct-wave interferometry is the retrieval of seismic surface waves between seismometers from ambient noise (Campillo & Paul 2003; Shapiro & Campillo 2004; Shapiro *et al.* 2005; Sabra *et al.* 2005a,b; Larose *et al.* 2006; Gerstoft *et al.* 2006; Yao *et al.* 2006; Bensen *et al.* 2007, 2008; Yao *et al.* 2008; Gouédard *et al.* 2008; Liang & Langston 2008; Ma *et al.* 2008; Lin *et al.* 2009; Picozzi *et al.* 2009). Usually one considers the retrieval of the fundamental mode only. It is well known that in a layered medium, surface waves consist of a fundamental mode and higher-order modes [e.g. Nolet (1975),Gabriels *et al.* (1987)]. Halliday & Curtis (2008) and Kimman & Trampert (2010) carefully analyse interferometry of surface waves with higher-order modes. They show that, when the primary sources are confined to the surface, crosscorrelation gives rise to spurious interferences between higher-order modes and the fundamental mode, whereas the presence of sources at depth, as prescribed by the theory (Wapenaar & Fokkema 2006), enables the correct recovery of all modes independently. In realistic situations the source distribution is mainly confined to the surface, which explains why in the current practice of surface-wave interferometry only the fundamental modes are properly retrieved.

In agreement with the current practice of surface-wave interferometry, in the following numerical example we consider fundamental Rayleigh-wave modes only. These modes can be treated as the solution of a scalar 2-D wave equation with the propagation velocity being the dispersive Rayleigh wave velocity of the layered medium. Hence, for interferometry we can make use of the 2-D version of the scalar Green's function representations, discussed in the theory sections. The basic configuration is shown in Fig. 2(a) for the crosscorrelation method, and in Fig. 3(a) for the MDD method. For the current purpose these figures should be seen as plan views.

Consider Fig. 10(a), which shows a map of the USA, 38 receiver stations of the USArray (green triangles) and 242 sources along the East coast (blue dots), for example, representing storm-related microseismic sources (Bromirski 2001). Moreover, the black dot denotes a strong scatterer, representing the Yellowstone plume (Smith *et al.* 2009). Assuming a layered medium, we compute the dispersion curve of the fundamental mode of the Rayleigh-wave for the upper 300 km of the PREM model (Dziewonski & Anderson 1981), using the approach described by Wathelet *et al.* (2004). The dispersion curve is shown in Fig. 10(b). We define the sources as simultaneously acting uncorrelated noise sources, with a central frequency of 0.04 Hz. Using the computed dispersion curve, we model the surface-wave response of the distribution of noise sources at all indicated receivers. Fig. 10(c) shows 1500 s of the response along the indicated South–North array in central USA (the total duration of the modelled noise responses is approximately 2 days).

Our aim is to turn one of the receivers of the South–North array (the one indicated by the red triangle) into a virtual source and to retrieve the response of this virtual source at the irregular receiver stations in the Western USA. Following the crosscorrelation method we take the noise response at the red receiver and crosscorrelate it with each of the responses at the receivers in the Western USA, that is, we evaluate $\langle u(\mathbf{x}_B, t) * u(\mathbf{x}_A, -t)\rangle$, with $\mathbf{x}_A$ fixed at the red receiver and $\mathbf{x}_B$ variable. The result is shown in Fig. 11(a) by the red traces. For comparison, the black traces in this figure represent the directly modelled surface-wave response of a source at the position of the red receiver, using a source function $S(t)$ equal to the average autocorrelation of the noise. There is a pronounced mismatch between the red and black waveforms, as a result of the irregularity of the source distribution. Overall, the amplitudes of the direct wave are estimated too high, whereas the amplitudes of the scattered event are underestimated.

For the MDD approach we need to invert eq. (27), with, according to eq. (31), the correlation function given by $C(\mathbf{x}_B, \mathbf{x}_A, t) = \langle u(\mathbf{x}_B, t) * u^{\mathrm{in}}(\mathbf{x}_A, -t)\rangle$, and, according to eq. (32), the point-spread function given by $\Gamma(\mathbf{x}, \mathbf{x}_A, t) = \langle u^{\mathrm{in}}(\mathbf{x}, t) * u^{\mathrm{in}}(\mathbf{x}_A, -t)\rangle$. These expressions contain the inward propagating waves at $\mathbf{x}$ and $\mathbf{x}_A$ on $\mathbb{S}_{\mathrm{rec}}$ (which corresponds with the South–North array). Because we consider noise responses we cannot separate the inward propagating waves u^{in} from the outward propagating waves u^{out} by time-windowing. If we would have multicomponent receivers or two arrays close to each other, we could apply decomposition, after which $C(\mathbf{x}_B, \mathbf{x}_A, t)$ and $\Gamma(\mathbf{x}, \mathbf{x}_A, t)$ could be evaluated. In the following, we assume that these conditions for decomposition are not fulfilled. Although separation by time-windowing cannot be applied to the noise data, it can be applied to the correlation function. Recall that Fig. 11(a) represents the correlation of full wavefields, that is, $\langle u(\mathbf{x}_B, t) * u(\mathbf{x}_A, -t)\rangle$. From this we extract $\langle u(\mathbf{x}_B, t) * u^{\mathrm{in}}(\mathbf{x}_A, -t)\rangle$ by removing the events in the grey-shaded area as well as all events at negative time (not shown in Fig. 11a), which together represent $\langle u(\mathbf{x}_B, t) * u^{\mathrm{out}}(\mathbf{x}_A, -t)\rangle$. Hence, we retain only the green-shaded area in Fig. 11(a), representing $C(\mathbf{x}_B, \mathbf{x}_A, t) = \langle u(\mathbf{x}_B, t) * u^{\mathrm{in}}(\mathbf{x}_A, -t)\rangle$. To obtain the point-spread function, we first evaluate $\langle u(\mathbf{x}, t) * u(\mathbf{x}_A, -t)\rangle$, with $\mathbf{x}_A$ again fixed at the red receiver and $\mathbf{x}$ variable along the South–North array, see Fig. 11(b). We remove the events in the white area, representing $\langle u^{\mathrm{out}}(\mathbf{x}, t) * u^{\mathrm{in}}(\mathbf{x}_A, -t)\rangle$, and those in the grey-shaded area, representing $\langle u^{\mathrm{in}}(\mathbf{x}, t) * u^{\mathrm{out}}(\mathbf{x}_A, -t)\rangle$. We retain the green-shaded area, representing $\langle u^{\mathrm{in}}(\mathbf{x}, t) * u^{\mathrm{in}}(\mathbf{x}_A, -t)\rangle + \langle u^{\mathrm{out}}(\mathbf{x}, t) * u^{\mathrm{out}}(\mathbf{x}_A, -t)\rangle$. Assuming the outward propagating field is relatively small, we may thus approximate the events in the green-shaded area in Fig. 11(b) by $\Gamma(\mathbf{x}, \mathbf{x}_A, t) = \langle u^{\mathrm{in}}(\mathbf{x}, t) * u^{\mathrm{in}}(\mathbf{x}_A, -t)\rangle$. We are now

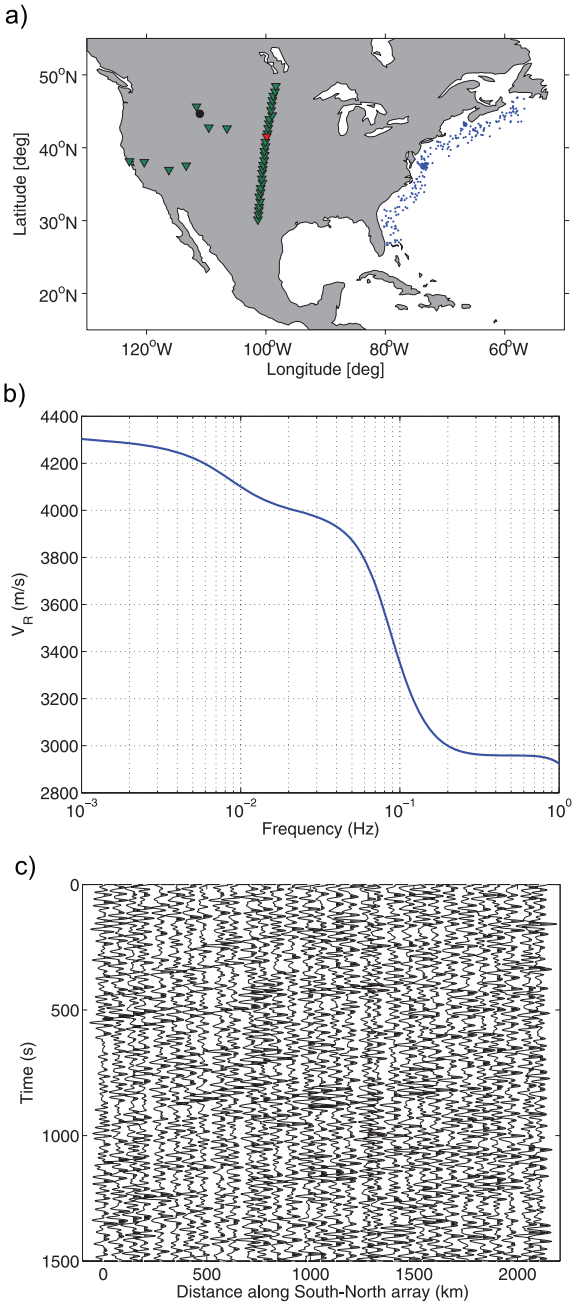

Figure 10. Model for passive surface-wave interferometry. (a) Map of USA, with USArray stations (green triangles), storm-related microseismic sources (blue dots) and a scatterer (black dot). (b) Rayleigh-wave dispersion curve (fundamental mode), based on the PREM model. (c) Modelled Rayleigh-wave response along South–North array in central USA.

ready to apply MDD, which involves inversion of eq. (27), that is, removing the effect of the point-spread function (the green-shaded area in Fig. 11b) from the correlation function (the green-shaded area in Fig. 11a). The result is shown by the red traces in Fig. 11(c), for display purposes convolved with $S(t)$. Note that the waveforms of the direct wave as well as those of the scattered wave match the directly modelled waveforms (the black traces) much better than in Fig. 11(a). We also observe some non-causal residues at small traveltimes. These are mainly due to the fact that time-windowing is an imperfect method to separate events in the correlation functions. To reduce the amount of required time-windowing, we propose to replace eqs (31) and (32) by

$$C(\mathbf{x}_B, \mathbf{x}_A, t) = \langle u(\mathbf{x}_B, t) * u(\mathbf{x}_A, -t) \rangle, \tag{59}$$

$$\Gamma(\mathbf{x}, \mathbf{x}_A, t) = \langle u^{\mathrm{in}}(\mathbf{x}, t) * u(\mathbf{x}_A, -t) \rangle \, . \tag{60}$$

Note that in both equations we made the same replacement, that is, we replaced $u^{\mathrm{in}}(\mathbf{x}_A, -t)$ by $u(\mathbf{x}_A, -t)$. Hence, eq. (27) holds with the correlation and point-spread function defined by eqs (59) and (60), respectively. The correlation function is obtained from full wavefields,

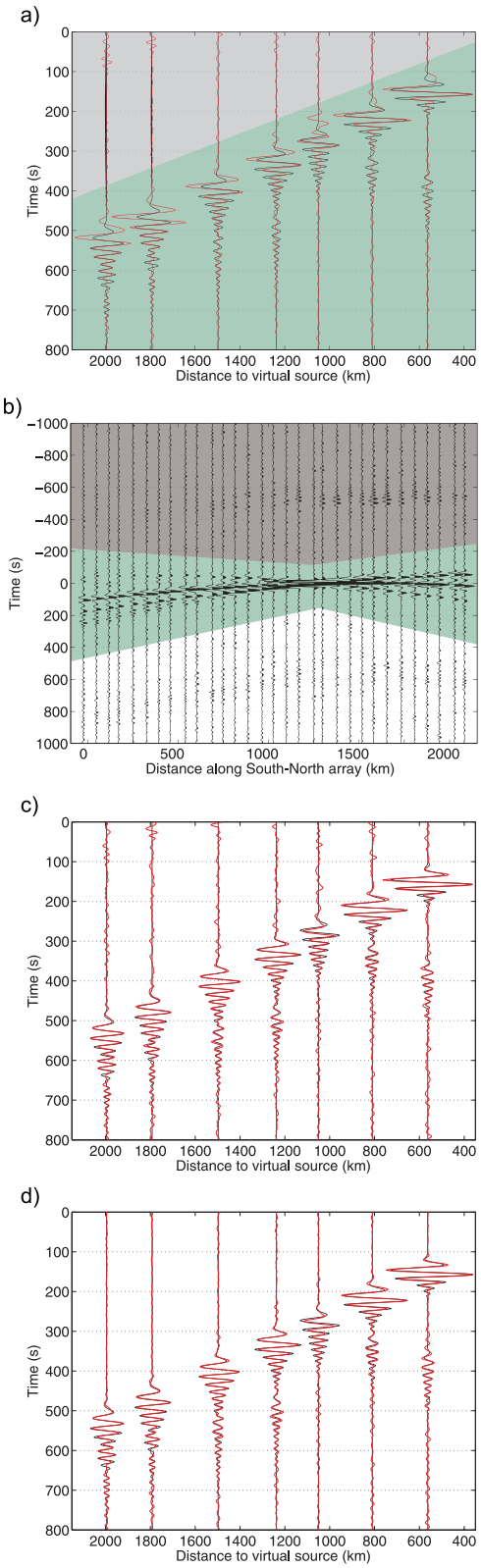

Figure 11. Passive surface-wave interferometry. (a) Crosscorrelation result (red) compared with directly modelled response (black). The virtual source is indicated by the red receiver in Fig. 10(a). The traces correspond to the irregular receiver stations in the Western USA in Fig. 10(a). (b) Green-shaded area: approximation of the point-spread function along the South–North array. (c) MDD result (red) compared with directly modelled response (black). (d) As in (c), but obtained from correlation and point-spread function defined by eqs (59) and (60).

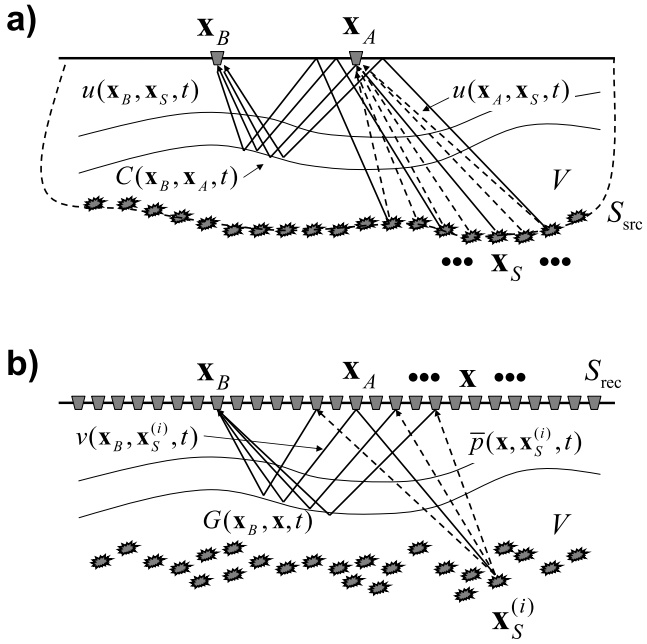

Figure 12. Configurations for passive body-wave interferometry. (a) In the crosscorrelation method the full wavefields $u(\mathbf{x}_A, \mathbf{x}_S, t)$ and $u(\mathbf{x}_B, \mathbf{x}_S, t)$ are correlated and integrated along the sources on $\mathbb{S}_{\mathrm{src}}$. The correlation function $C(\mathbf{x}_B, \mathbf{x}_A, t)$ is proportional to $G(\mathbf{x}_B, \mathbf{x}_A, t) + G(\mathbf{x}_B, \mathbf{x}_A, -t)$, convolved with the autocorrelation of the sources. (b) The convolutional model used for interferometry by MDD. The response $v(\mathbf{x}_B, \mathbf{x}_S^{(i)}, t) - \bar{v}(\mathbf{x}_B, \mathbf{x}_S^{(i)}, t)$ is equal to the convolution of the Green's function $G(\mathbf{x}_B, \mathbf{x}, t)$ and the reference wavefield $\bar{p}(\mathbf{x}, \mathbf{x}_S^{(i)}, t)$, integrated along the receivers at $\mathbb{S}_{\mathrm{rec}}$.

hence no time windowing is needed in Fig. 11(a). The point-spread function now consists of $\langle u^{\mathrm{in}}(\mathbf{x}, t) * u^{\mathrm{in}}(\mathbf{x}_A, -t)\rangle + \langle u^{\mathrm{in}}(\mathbf{x}, t) * u^{\mathrm{out}}(\mathbf{x}_A, -t)\rangle$, hence, only the events in the white area in Fig. 11(b) need to be removed to obtain an approximation of $\Gamma(\mathbf{x}, \mathbf{x}_A, t)$. Applying MDD by inverting eq. (27), with the correlation and point-spread function defined by eqs (59) and (60), respectively, we obtain the result shown by the red traces in Fig. 11(d) (for display purposes convolved with $S(t)$). Note that the match with the directly modelled result is again very good and that the non-causal residuals vanished almost completely.

6.2 Passive body-wave interferometry

Ambient noise is usually dominated by surface waves. Passive body-wave interferometry is only possible after careful suppression of surface waves (Draganov *et al.* 2009).

Fig. 12(a) shows the configuration for passive body-wave interferometry by crosscorrelation. The surface $\mathbb{S}_{\mathrm{src}}$ forms together with the Earth's free surface a closed boundary. Sources are only required on the open surface $\mathbb{S}_{\mathrm{src}}$. The correlation function $C(\mathbf{x}_B, \mathbf{x}_A, t)$ involves the crosscorrelation of the full wavefields at $\mathbf{x}_A$ and $\mathbf{x}_B$ [Fig. 12a only shows the direct path of $u(\mathbf{x}_A, \mathbf{x}_S, t)$ and the first reflected path of $u(\mathbf{x}_B, \mathbf{x}_S, t)$]. The crosscorrelation is integrated over the source positions in case of transient sources (eq. 11) or averaged over time in case of uncorrelated noise sources (eq. 17). Eq. (13) gives the relation between the correlation function $C(\mathbf{x}_B, \mathbf{x}_A, t)$ and the Green's function $G(\mathbf{x}_B, \mathbf{x}_A, t)$, which for the current configuration should be interpreted as the reflection response of the subsurface. It includes primary and multiple reflections (internal multiples and surface-related multiples) as well as a direct wave. Eqs (11), (13) and (17) have been derived for the situation that the receivers $\mathbf{x}_A$ and $\mathbf{x}_B$ are in $\mathbb{V}$. In that case, u stands for acoustic pressure (p) and $G(\mathbf{x}_B, \mathbf{x}_A, t)$ represents the acoustic pressure at $\mathbf{x}_B$ due to an impulsive point source of volume injection rate at source position $\mathbf{x}_A$. The equations remain valid when the receivers $\mathbf{x}_A$ and $\mathbf{x}_B$ are at the free surface. In that case u stands for the normal particle velocity (v) and $G(\mathbf{x}_B, \mathbf{x}_A, t)$ represents the normal particle velocity at $\mathbf{x}_B$ due to an impulsive normal traction source at $\mathbf{x}_A$ (Wapenaar & Fokkema 2006).

We illustrate this method with a numerical example. Consider the configuration in Fig. 13(a), which consists of a horizontally layered target below a homogeneous overburden. The green triangles at the free surface denote 51 regularly spaced vertical geophones with spacing $\Delta x_1 = 40$ m (only nine geophones are shown). The blue dots below the layered target denote 250 irregularly spaced uncorrelated noise sources with an average lateral spacing of $\Delta x_1 = 20$ m and a central frequency of 22 Hz. Note the clustering of sources around $x_1 \approx -1400$ m and $x_1 \approx 500$ m. The responses of these sources are shown in Fig. 13(b) (only 3 s of 25 min of noise is shown). We denote these responses as $v(\mathbf{x}_A, t)$ and $v(\mathbf{x}_B, t)$, where $\mathbf{x}_A$ and $\mathbf{x}_B$ can be any of the 51 geophones. We evaluate the correlation function

$$C_{v,v}(\mathbf{x}_B, \mathbf{x}_A, t) = \langle v(\mathbf{x}_B, t) * v(\mathbf{x}_A, -t)\rangle, \tag{61}$$

averaged over 25 min of noise. The result is shown in Fig. 13(c) for fixed $\mathbf{x}_A$ (geophone number 26) and variable $\mathbf{x}_B$ (geophones $1 - 51$). According to eq. (13) this correlation function is proportional to $\{G(\mathbf{x}_B, \mathbf{x}_A, t) + G(\mathbf{x}_B, \mathbf{x}_A, -t)\} * S(t)$. Fig. 13(d) shows a zoomed version

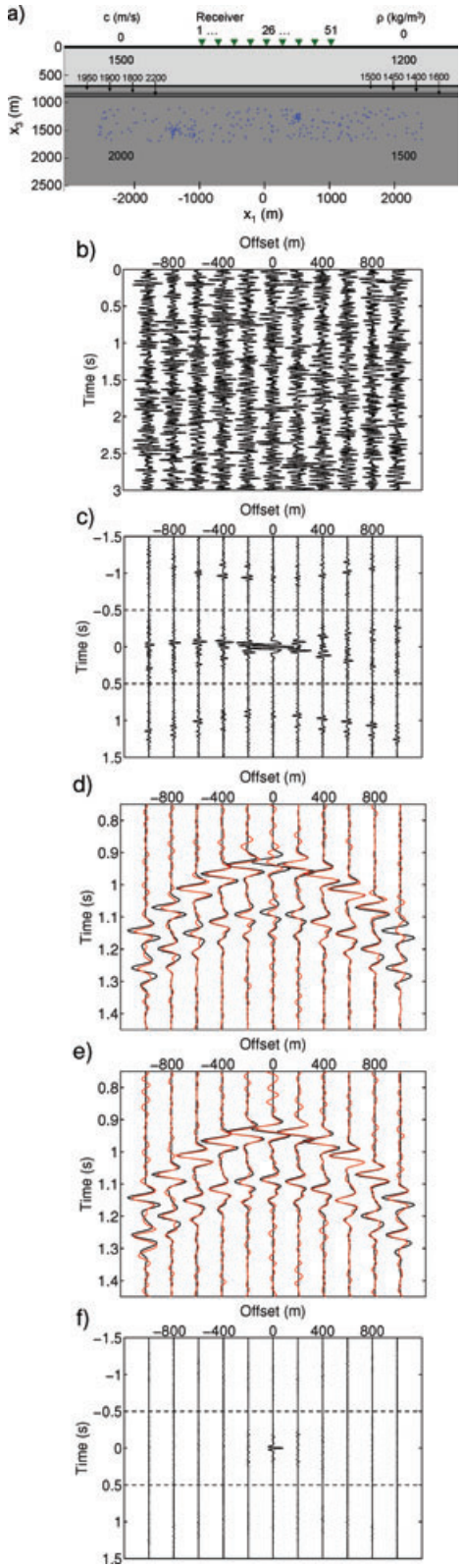

Figure 13. Numerical example of ambient-noise body-wave interferometry. (a) Configuration with a horizontally layered target below a homogeneous overburden and a free surface. There is an irregular distribution of uncorrelated noise sources below the target. (b) Modelled noise response, observed by receivers at the free surface. (c) Correlation function $C_{v,v}(\mathbf{x}_B, \mathbf{x}_A, t) = \langle v(\mathbf{x}_B, t) * v(\mathbf{x}_A, -t)\rangle$ (fixed $\mathbf{x}_A$, variable $\mathbf{x}_B$), clipped at 20 per cent of the maximum amplitude. (d) Zoomed version of the causal part of the correlation function (red traces), compared with the directly modelled scattered part of the Green's function, $G^s(\mathbf{x}_B, \mathbf{x}_A, t) * S(t)$. (e) Idem, for the MDD result. This was obtained by deconvolving the causal events in (c) by the point-spread function (the strong event in (c) around $t = 0$). (f) Directly modelled correlation function $C_{v^s,v^s}(\mathbf{x}_B, \mathbf{x}_A, t)$ (same amplitude scaling as in c). This weak event is ignored in the MDD method.

of the causal part of the correlation function $C_{v,v}(\mathbf{x}_B, \mathbf{x}_A, t)$ (the red traces) and the directly modelled reflection response $G^{\mathrm{s}}(\mathbf{x}_B, \mathbf{x}_A, t) * S(t)$ with the source $\mathbf{x}_A$ at the position of geophone 26 (the black traces). Here $G^{\mathrm{s}}(\mathbf{x}_B, \mathbf{x}_A, t)$ is the scattered Green's function, that is, the total Green's function $G(\mathbf{x}_B, \mathbf{x}_A, t)$ minus the direct wave. Note that the arrival times of the correlation function nicely match those of the directly modelled reflection response, but the waveforms and amplitudes are not accurately reconstructed. This discrepancy is a consequence of the irregular source distribution, in particular the clustering around $x_1 \approx -1400$ m and $x_1 \approx 500$ m (Fig. 13a), which implies that the integral along $\mathbb{S}_{\mathrm{src}}$ is not properly discretized.

Next, we discuss passive reflected-wave interferometry by MDD. Fig. 12(b) shows the modified configuration. This configuration is different from other MDD configurations discussed in this paper in the sense that the source positions $\mathbf{x}_S^{(i)}$ are now in $\mathbb{V}$. Hence, because this configuration is not a special case of that in Fig. 1(b) we cannot make use of eq. (26) without making some modifications. We previously dealt with the configuration of Fig. 12(b) (Wapenaar *et al.* 2008b) and derived the following convolution-type representation

$$v\left(\mathbf{x}_B, \mathbf{x}_S^{(i)}, t\right) - \bar{v}\left(\mathbf{x}_B, \mathbf{x}_S^{(i)}, t\right) = \int_{\mathbb{S}_{\mathrm{rec}}} G(\mathbf{x}_B, \mathbf{x}, t) * \bar{p}\left(\mathbf{x}, \mathbf{x}_S^{(i)}, t\right) \mathrm{d}\mathbf{x}. \tag{62}$$

Here the bars denote a reference situation with absorbing boundary conditions at $\mathbb{S}_{\mathrm{rec}}$. Hence, $\bar{p}(\mathbf{x}, \mathbf{x}_S^{(i)}, t)$ and $\bar{v}(\mathbf{x}_B, \mathbf{x}_S^{(i)}, t)$ are the pressure and normal particle velocity that would be measured at $\mathbb{S}_{\mathrm{rec}}$ in absence of the free surface. The Green's function $G(\mathbf{x}_B, \mathbf{x}, t)$ in eq. (62) represents again the normal particle velocity at $\mathbf{x}_B$ due to an impulsive normal traction source at source position $\mathbf{x}$, both at $\mathbb{S}_{\mathrm{rec}}$. It is defined in the actual medium with the free-surface boundary condition at $\mathbb{S}_{\mathrm{rec}}$. For later convenience we subtract the direct wave contribution from both sides of eq. (62), yielding

$$v^{\mathrm{s}}\left(\mathbf{x}_B, \mathbf{x}_S^{(i)}, t\right) = \int_{\mathbb{S}_{\mathrm{rec}}} G^{\mathrm{s}}\left(\mathbf{x}_B, \mathbf{x}, t\right) * \bar{p}\left(\mathbf{x}, \mathbf{x}_S^{(i)}, t\right) \mathrm{d}\mathbf{x}, \tag{63}$$

where $G^{\mathrm{s}}(\mathbf{x}_B, \mathbf{x}, t)$ is again the scattered Green's function (i.e. the total Green's function minus the direct wave) and where

$$v^{\mathrm{s}}\left(\mathbf{x}_B, \mathbf{x}_S^{(i)}, t\right) = v\left(\mathbf{x}_B, \mathbf{x}_S^{(i)}, t\right) - 2\bar{v}\left(\mathbf{x}_B, \mathbf{x}_S^{(i)}, t\right). \tag{64}$$

The factor two reflects the fact that the direct wave in $v(\mathbf{x}_B, \mathbf{x}_S^{(i)}, t)$ is twice the direct wave $\bar{v}(\mathbf{x}_B, \mathbf{x}_S^{(i)}, t)$ in the situation without free surface. Note that, despite the differences with eq. (26), the form of eq. (63) is the same as that of eq. (26). Hence, analogous to eq. (27) we may write

$$C_{v^{\mathrm{s}},\bar{v}}(\mathbf{x}_B, \mathbf{x}_A, t) = \int_{\mathbb{S}_{\mathrm{rec}}} G^{\mathrm{s}}(\mathbf{x}_B, \mathbf{x}, t) * \Gamma(\mathbf{x}, \mathbf{x}_A, t) \, \mathrm{d}\mathbf{x}, \tag{65}$$

where the correlation function and the point-spread function are defined as

$$C_{v^{\mathrm{s}},\bar{v}}(\mathbf{x}_B, \mathbf{x}_A, t) = \sum_i v^{\mathrm{s}}\left(\mathbf{x}_B, \mathbf{x}_S^{(i)}, t\right) * \bar{v}\left(\mathbf{x}_A, \mathbf{x}_S^{(i)}, -t\right), \tag{66}$$

$$\Gamma(\mathbf{x}, \mathbf{x}_A, t) = \sum_i \bar{p}\left(\mathbf{x}, \mathbf{x}_S^{(i)}, t\right) * \bar{v}\left(\mathbf{x}_A, \mathbf{x}_S^{(i)}, -t\right) \tag{67}$$

in the case of transient sources, or as

$$C_{v^{\mathrm{s}},\bar{v}}(\mathbf{x}_B, \mathbf{x}_A, t) = \langle v^{\mathrm{s}}(\mathbf{x}_B, t) * \bar{v}(\mathbf{x}_A, -t)\rangle, \tag{68}$$

$$\Gamma(\mathbf{x}, \mathbf{x}_A, t) = \langle \bar{p}(\mathbf{x}, t) * \bar{v}(\mathbf{x}_A, -t)\rangle \tag{69}$$

in the case of uncorrelated noise sources. A complication is that these correlation functions contain fields in a reference situation with an absorbing boundary at $\mathbb{S}_{\mathrm{rec}}$. To see how this can be dealt with for transient sources and for noise sources, consider again the configuration of Fig. 13(a). When the sources are transients, the first arrivals (including internal multiple scattering in the target) in $v(\mathbf{x}_A, \mathbf{x}_S^{(i)}, t)$ are well separated in time from the surface-related multiples, so the reference response $\bar{v}(\mathbf{x}_A, \mathbf{x}_S^{(i)}, t)$ can be extracted by applying a time window to $v(\mathbf{x}_A, \mathbf{x}_S^{(i)}, t)$ and multiplying the result by one-half. Both $\bar{v}$ and $\bar{p}$ are outward-propagating waves at the absorbing boundary $\mathbb{S}_{\mathrm{rec}}$, so $\bar{p}$ can be obtained from $\bar{v}$ using the equation of motion and the one-way wave equation for outward-propagating waves, according to

$$-j\omega\rho\hat{\bar{v}} = n_i \partial_i \hat{\bar{p}} = -j\hat{\mathcal{H}}_1 \hat{\bar{p}}. \tag{70}$$

Because of the near-vertical incidence of the waves at $\mathbb{S}_{\mathrm{rec}}$, in practice it suffices to make the following approximation

$$\bar{p}\left(\mathbf{x}, \mathbf{x}_S^{(i)}, t\right) \approx \rho_1 c_1 \bar{v}\left(\mathbf{x}, \mathbf{x}_S^{(i)}, t\right), \tag{71}$$

where ρ_1 and c_1 are the mass density and propagation velocity, respectively, directly below $\mathbb{S}_{\mathrm{rec}}$. This gives all fields needed in eqs (64), (66) and (67) to evaluate the correlation function and the point-spread function, after which $G^{\mathrm{s}}(\mathbf{x}_B, \mathbf{x}, t)$ can be resolved by MDD from eq. (65), see Wapenaar *et al.* (2008b) for a numerical example.

When the sources are noise sources we cannot separate the reference fields from the measured fields by time windowing, but van der Neut *et al.* (2010) propose to make such a separation in the correlation function, as follows. Using $v = 2\bar{v} + v^{\mathrm{s}}$ (eq. 64) we write for the correlation function, as defined in eq. (61),

$$C_{v,v}(\mathbf{x}_B, \mathbf{x}_A, t) = \{4C_{\bar{v},\bar{v}} + 2C_{v^{\mathrm{s}},\bar{v}} + 2C_{\bar{v},v^{\mathrm{s}}} + C_{v^{\mathrm{s}},v^{\mathrm{s}}}\}(\mathbf{x}_B, \mathbf{x}_A, t), \tag{72}$$

with $C_{v^{\mathrm{s}},\bar{v}}(\mathbf{x}_B, \mathbf{x}_A, t)$ defined in eq. (68), and

$$C_{\bar{v},\bar{v}}(\mathbf{x}_B, \mathbf{x}_A, t) = \langle \bar{v}(\mathbf{x}_B, t) * \bar{v}(\mathbf{x}_A, -t)\rangle, \tag{73}$$

$$C_{\bar{v},v^{\rm s}}(\mathbf{x}_B, \mathbf{x}_A, t) = \langle \bar{v}(\mathbf{x}_B, t) * v^{\rm s}(\mathbf{x}_A, -t) \rangle, \tag{74}$$

$$C_{v^{\rm s},v^{\rm s}}(\mathbf{x}_B, \mathbf{x}_A, t) = \langle v^{\rm s}(\mathbf{x}_B, t) * v^{\rm s}(\mathbf{x}_A, -t) \rangle\,. \tag{75}$$

For the configuration of Fig. 13(a), the total correlation function $C_{v,v}(\mathbf{x}_B, \mathbf{x}_A, t)$ is shown in Fig. 13(c) (for fixed $\mathbf{x}_A$ and variable $\mathbf{x}_B$). Assuming $C_{v^{\rm s},v^{\rm s}}(\mathbf{x}_B, \mathbf{x}_A, t)$ is weak, the other three terms can be easily obtained from Fig. 13(c). The strong event between the two dashed lines is the correlation of the reference response, $4C_{\bar{v},\bar{v}}(\mathbf{x}_B, \mathbf{x}_A, t)$. The causal event (below the lower dashed line) is $2C_{v^{\rm s},\bar{v}}(\mathbf{x}_B, \mathbf{x}_A, t)$ and the acausal event (above the upper dashed line) is $2C_{\bar{v},v^{\rm s}}(\mathbf{x}_B, \mathbf{x}_A, t)$. To invert eq. (65), we also need $\Gamma(\mathbf{x}, \mathbf{x}_A, t)$, defined in eq. (69). Analogous to eq. (70), this can be obtained from

$$-j\omega\rho C_{\bar{v},\bar{v}}(\mathbf{x}, \mathbf{x}_A, t) = -j\hat{\mathcal{H}}_1 \Gamma(\mathbf{x}, \mathbf{x}_A, t). \tag{76}$$

Assuming again near-vertical incidence, this can be approximated by

$$\Gamma(\mathbf{x}, \mathbf{x}_A, t) \approx \rho_1 c_1 C_{\bar{v},\bar{v}}(\mathbf{x}, \mathbf{x}_A, t). \tag{77}$$

Having determined these functions, $G^{\rm s}(\mathbf{x}_B, \mathbf{x}, t)$ can again be resolved from eq. (65) by MDD. The result (for $\mathbf{x} = \mathbf{x}_A$ fixed at the central geophone and variable $\mathbf{x}_B$) is shown in Fig. 13(e) (red traces), where it is compared with the directly modelled scattered Green's function (black traces). Both results have been convolved with $S(t)$ to facilitate the comparison with the correlation of Fig. 13(d). The MDD result in Fig. 13(e) matches the directly modelled response significantly better than the correlation in Fig. 13(d).

Note that we assumed that $C_{v^{\rm s},v^{\rm s}}(\mathbf{x}_B, \mathbf{x}_A, t)$ is weak. Fig. 13(f) shows this function obtained from direct modelling and displayed with the same amplitude scaling as $C_{v,v}(\mathbf{x}_B, \mathbf{x}_A, t)$ in Fig. 13(c). We observe that for this example it is indeed weak. The main contribution is concentrated around $t = 0$, so it has only a small effect on the estimated point-spread function, which is obtained [via eqs (73) and (77)] from the event between the dashed lines in Fig. 13(c). When there are strong reflectors in the subsurface, $C_{v^{\rm s},v^{\rm s}}(\mathbf{x}_B, \mathbf{x}_A, t)$ may not be weak and distort the estimation of the point-spread function.

An alternative deconvolution approach for passive reflected-wave interferometry is presented by van Groenestijn & Verschuur (2010). Their method does not use the separation of events in the correlation function, but is adaptive and aims to minimize the energy in the estimated reference wavefield $\bar{v}(\mathbf{x}_A, t)$. Since the reflections in the total noise field $v(\mathbf{x}_A, t)$ may interfere constructively as well as destructively with the reference noise field $\bar{v}(\mathbf{x}_A, t)$, there is no physical justification that the energy in $\bar{v}(\mathbf{x}_A, t)$ should be minimized. It remains an open question which of the approaches functions best in case of strongly scattering media.

7 DISCUSSION AND CONCLUSIONS

The methodology of seismic interferometry (or Green's function retrieval) by crosscorrelation has a number of attractive properties as well as several limitations. The main attractiveness of the method is that a deterministic medium response can be obtained from controlled-source or passive noise measurements, without the need to know the medium parameters nor the positions of the sources. The fact that this deterministic response is obtained by a straightforward crosscorrelation of two receiver responses has also contributed to the popularity of the method. The main underlying assumptions are that the medium is lossless and that the wavefield is equipartitioned, meaning that the net power-flux is (close to) zero (Malcolm *et al.* 2004; Sánchez-Sesma *et al.* 2006). It has been shown by Fan & Snieder (2009) that equipartitioning is a necessary but not a sufficient condition.

For open systems the method works well when the receivers that are used in the correlation process are surrounded by a regular distribution of independent transient or uncorrelated noise sources with equal autocorrelation functions. However, in practical situations the method may suffer from irregularities in the source distribution, asymmetric illumination, intrinsic losses, etc.

Figs 3(a) and (b) illustrate configurations with an irregular source distribution in a finite region, illuminating the medium from one side only. For these configurations, eq. (27) shows that the crosscorrelation function $C(\mathbf{x}_B, \mathbf{x}_A, t)$ is a distorted version of the sought Green's function $\bar{G}_{\rm d}(\mathbf{x}_B, \mathbf{x}, t)$. The distortion is quantified by the interferometric point-spread function $\Gamma(\mathbf{x}, \mathbf{x}_A, t)$, which blurs the source of the Green's function in the spatial directions and generates ghosts in the temporal direction (van der Neut & Thorbecke 2009). As such, this interferometric point-spread function plays a similar role as the point-spread function in optical, acoustic and seismic imaging systems (Born & Wolf 1965; Norton 1992; Schuster & Hu 2000). When the point-spread function of an imaging system is known, the resolution of an image can be improved by deconvolving for the point-spread function (Jansson 1997; Hu *et al.* 2001). For example, early images of the Hubble Space Telescope were blurred by a flaw in the mirror. These images were sharpened by deconvolving for the point-spread function of the flawed mirror (Boden *et al.* 1996). In a similar way, the blurred source with ghosts of the Green's function obtained by crosscorrelation can be deblurred and deghosted by deconvolving for the interferometric point-spread function, that is, by inverting eq. (27) by MDD. An interesting aspect is that the interferometric point-spread function can be obtained directly from measured responses, hence, it does not require knowledge of the complex medium nor of the sources. This means that it automatically accounts for the distorting effects of the irregularity of the sources (including variations in their autocorrelation functions), and of the medium inhomogeneities, including multiple scattering.

The MDD method has, of course, also its limitations. First, to retrieve the Green's function $\bar{G}_{\rm d}(\mathbf{x}_B, \mathbf{x}, t)$ it does not suffice to have two receivers only, at $\mathbf{x}$ and $\mathbf{x}_B$, because $\mathbf{x}$ is assumed to be an element of a regular (or regularized) array of receivers along $\mathbb{S}_{\rm rec}$, see Fig. 3. Secondly, the expressions for the correlation function (eqs 28 and 31) and for the point-spread function (eqs 29 and 32) contain the inward-propagating field $u^{\rm in}(\mathbf{x}, t)$ on $\mathbb{S}_{\rm rec}$ (propagating into $\mathbb{V}$). To extract this inward-propagating field from the total field, either multicomponent receivers or two

receiver surfaces close to each other are required. Alternatively, when the scattering is weak, one could correlate the total fields and extract the point-spread function by applying a time window around $t = 0$. Thirdly, MDD involves an inversion of an integral equation, which in practice is achieved by matrix inversion. This matrix inversion can be unstable. The well-posedness of this inverse problem depends on the number of available sources, the source aperture, the bandwidth and, for multicomponent data, on the number of independent source components. In practical situations a spectral analysis of the point-spread function helps to assess for which spatial and temporal frequencies the inversion can be carried out in a stable sense (van der Neut *et al.* 2011). Finally, because of the matrix inversion, the costs of the MDD method are higher than those of the correlation method. For the 2-D examples in this paper, the costs of the matrix inversions were moderate, despite the fact that we used direct solvers only. For 3-D applications we expect that MDD is still feasible, particularly when use is made of iterative solvers.

Despite the mentioned limitations, for applications in which the data are measured with arrays of receivers, Green's function retrieval by MDD has the potential to obtain virtual sources that are better focused and have less distortions by spurious multiples than those obtained by crosscorrelation.

ACKNOWLEDGMENTS

This work is supported by the Netherlands Research Centre for Integrated Solid Earth Science (ISES), The Netherlands Organisation for Scientific Research (NWO, Toptalent 2006 AB), and the Dutch Technology Foundation STW (grants VENI.08115 and DCB.7913). We thank associate editor Andrew Curtis and two anonymous reviewers for their constructive comments and suggestions, which helped to improve this paper.

REFERENCES

Amundsen, L., 2001. Elimination of free-surface related multiples without need of the source wavelet, *Geophysics,* **66**(1), 327–341.

Amundsen, L. & Reitan, A., 1995. Decomposition of multicomponent seafloor data into upgoing and downgoing P- and S-waves, *Geophysics,* **60,** 563–572.

Amundsen, L., Løseth, L., Mittet, R., Ellingsrud, S. & Ursin, B., 2006. Decomposition of electromagnetic fields into upgoing and downgoing components, *Geophysics,* **71**(5), G211–G223.

Bagaini, C., 2006. Overview of simultaneous Vibroseis acquisition methods, in *Proc. 76th Annual Int. Meeting Soc. Expl. Geophys., Expanded Abstracts,* pp. 70–74, SEG, Tulsa, OK.

Bakulin, A. & Calvert, R., 2004. Virtual source: new method for imaging and 4D below complex overburden, in *Proc. 74th Annual Int. Meeting Soc. Expl. Geophys., Expanded Abstracts,* pp. 2477–2480, SEG, Tulsa, OK.

Bakulin, A. & Calvert, R., 2006. The virtual source method: theory and case study, *Geophysics,* **71**(4), SI139–SI150.

Beasley, C.J., Chambers, R.E. & Jiang, Z., 1998. A new look at simultaneous sources, in *Proc. 68th Annual Int. Meeting Soc. Expl. Geophys., Expanded Abstracts,* pp. 133–135, SEG, Tulsa, OK.

Bensen, G.D., Ritzwoller, M.H., Barmin, M.P., Levshin, A.L., Lin, F., Moschetti, M.P., Shapiro, N.M. & Yang, Y., 2007. Processing seismic ambient noise data to obtain reliable broad-band surface wave dispersion measurements, *Geophys. J. Int.,* **169,** 1239–1260.

Bensen, G.D., Ritzwoller, M.H. & Shapiro, N.M., 2008. Broadband ambient noise surface wave tomography across the United States, *J. geophys. Res.*, **113,** B05306, doi:10.1029/2007JB005248.

van den Berg, P.M., Abubakar, A. & Habashy, T.M., 2008. Removal of sea-surface-related wavefields and source replacement in CSEM data processing, in *Proc. 78th Annual Int. Meeting Soc. Expl. Geophys., Expanded Abstracts,* pp. 672–676, SEG, Tulsa, OK.

Berkhout, A.J., 1982. *Seismic Migration. Imaging of Acoustic Energy by Wave Field Extrapolation*, Elsevier, Amsterdam.

Berkhout, A.J., 1984. *Seismic Resolution. A Quantitative Analysis of Resolving Power of Acoustical Echo Techniques*, Geophysical Press, London.

Berkhout, A.J., 2008. Changing the mindset in seismic data acquisition, *Leading Edge,* **27**(7), 924–938.

Boden, A.F., Redding, D.C., Hanisch, R.J. & Mo, J., 1996. Massively parallel spatially variant maximum-likelihood restoration of Hubble Space Telescope imagery, *J. opt. Soc. Am.,* **13,** 1537–1545.

Born, M. & Wolf, E., 1965. *Principles of Optics,* Pergamon Press, London.

Bromirski, P.D., 2001. Vibrations from the "Perfect Storm", *Geochem. Geophys. Geosyst.,* **2,** 1030, doi:10.1029/2000GC000119.

Campillo, M. & Paul, A., 2003. Long-range correlations in the diffuse seismic coda, *Science,* **299,** 547–549.

Curtis, A. & Halliday, D., 2010. Directional balancing for seismic and general wavefield interferometry, *Geophysics,* **75**(1), SA1–SA14.

Draganov, D., Campman, X., Thorbecke, J., Verdel, A. & Wapenaar, K., 2009. Reflection images from ambient seismic noise, *Geophysics,* **74**(5), A63–A67.

Duijndam, A.J.W., Schonewille, M.A. & Hindriks, C.O.H., 1999. Reconstruction of band-limited signals, irregularly sampled along one spatial direction, *Geophysics,* **64,** 524–538.

Dziewonski, A.M. & Anderson, D.L., 1981. Preliminary reference Earth model, *Phys. Earth planet. Inter.,* **25,** 297–356.

Ellingsrud, S., Eidesmo, T., Johansen, S., Sinha, M.C., MacGregor, L.M. & Constable, S., 2002. Remote sensing of hydrocarbon layers by seabed logging (SBL): results from a cruise offshore Angola, *Leading Edge,* **21**(10), 972–982.

Esmersoy, C. & Oristaglio, M., 1988. Reverse-time wave-field extrapolation, imaging, and inversion, *Geophysics,* **53,** 920–931.

Fan, Y. & Snieder, R., 2009. Required source distribution for interferometry of waves and diffusive fields, *Geophys. J. Int.,* **179,** 1232–1244.

Fan, Y., Snieder, R. & Singer, J., 2009. 3-D controlled source electromagnetic (CSEM) interferometry by multi-dimensional deconvolution, in *Proc. 79th Annual Int. Meeting Soc. Expl. Geophys., Expanded Abstracts,* pp. 779–784, SEG, Tulsa, OK.

Fishman, L., 1993. One-way propagation methods in direct and inverse scalar wave propagation modeling, *Radio Sci.,* **28**(5), 865–876.

Fishman, L. & McCoy, J.J., 1984. Derivation and application of extended parabolic wave theories. I. The factorized Helmholtz equation, *J. Math. Phys.,* **25**(2), 285–296.

Frijlink, M. & Wapenaar, K., 2010. Reciprocity theorems for one-way wave fields in curvilinear coordinate systems, *SIAM J. Imaging Sci.,* **3**(3), 390–415.

Gabriels, P., Snieder, R. & Nolet, G., 1987. In situ measurements of shear-wave velocity in sediments with higher-mode Rayleigh waves, *Geophys. Prosp.,* **35,** 187–196.

Gelius, L.-J., Lecomte, I. & Tabti, H., 2002. Analysis of the resolution function in seismic prestack depth imaging, *Geophys. Prosp.,* **50,** 505–515.

Gerstoft, P., Sabra, K.G., Roux, P., Kuperman, W.A. & Fehler, M.C., 2006. Green's functions extraction and surface-wave tomography from microseisms in southern California, *Geophysics,* **71**(4), SI23–SI31.

Gouédard, P. *et al*., 2008. Cross-correlation of random fields: mathematical approach and applications, *Geophys. Prospect.,* **56,** 375–393.

van Groenestijn, G.J.A. & Verschuur, D.J., 2010. Estimation of primaries by sparse inversion from passive seismic data, *Geophysics,* **75**(4), SA61–SA69.

Halliday, D. & Curtis, A., 2008. Seismic interferometry, surface waves and source distribution, *Geophys. J. Int.,* **175,** 1067–1087.

Halliday, D. & Curtis, A., 2010. An interferometric theory of source-receiver scattering and imaging, *Geophysics,* **75**(6), SA95–SA103.

Hampson, G., Stefani, J. & Herkenhoff, F., 2008. Acquisition using simultaneous sources, *Leading Edge,* **27**(7), 918–923.

Howe, D., Foster, M., Allen, T., Taylor, B. & Jack, I., 2008. Independent simultaneous sweeping: a method to increase the productivity of land seismic crews, in *Proc. 78th Annual Int. Meeting Soc. Expl. Geophys., Expanded Abstracts,* pp. 2826–2830, SEG, Tulsa, OK.

Hu, J., Schuster, G.T. & Valasek, P., 2001. Poststack migration deconvolution, *Geophysics,* **66,** 939–952.

Hunziker, J., van der Neut, J., Slob, E. & Wapenaar, K., 2009. Controlled source interferometry with noisy data, in *Proc. 79th Annual Int. Meeting Soc. Expl. Geophys., Expanded Abstracts,* pp. 689–693, SEG, Tulsa, OK.

Hunziker, J., Fan, Y., Slob, E., Wapenaar, K. & Snieder, R., 2010. Solving spatial sampling problems in 2D-CSEM interferometry using elongated sources, in *EAGE, Extended Abstracts,* P083-1–P083-4, EAGE, Houten.

Ikelle, L., 2007. Coding and decoding: seismic data modeling, acquisition and processing, in *Proc. 77th Annual Int. Meeting Soc. Expl. Geophys., Expanded Abstracts,* pp. 66–70, SEG, Tulsa, OK.

Jansson, P., 1997. *Deconvolution of Images and Spectra,* Academic Press, San Diego.

Kimman, W.P. & Trampert, J., 2010. Approximations in seismic interferometry and their effects on surface waves, *Geophys. J. Int.,* **182,** 461–476.

Korneev, V. & Bakulin, A., 2006. On the fundamentals of the virtual source method, *Geophysics,* **71**(3), A13–A17.

Larose, E. *et al*., 2006. Correlation of random wave fields: an interdisciplinary review, *Geophysics,* **71**(4), SI11–SI21.

Lecomte, I., 2008. Resolution and illumination analyses in PSDM: a ray-based approach, *Leading Edge,* **27**(5), 650–663.

Liang, C. & Langston, C.A., 2008. Ambient seismic noise tomography and structure of eastern North America, *J. geophys. Res.,* **113,** B03309, doi:10.1029/2007JB005350.

Lin, F.-C., Ritzwoller, M.H. & Snieder, R., 2009. Eikonal tomography: surface wave tomography by phase front tracking across a regional broadband seismic array, *Geophys. J. Int.,* **177,** 1091–1110.

Ma, S., Prieto, G.A. & Beroza, G.C., 2008. Testing community velocity models for Southern California using the ambient seismic field, *Bull. seism. Soc. Am.,* **98,** 2694–2714.

Malcolm, A.E., Scales, J.A. & van Tiggelen, B.A., 2004. Extracting the Green function from diffuse, equipartitioned waves, *Phys. Rev. E,* **70,** 015601(R)-1–015601(R)-4.

van Manen, D.-J., Robertsson, J.O.A. & Curtis, A., 2005. Modeling of wave propagation in inhomogeneous media, *Phys. Rev. Lett.,* **94,** 164301, doi:10.1103/PhysRevLett.94.164301.

Mehta, K., Bakulin, A., Sheiman, J., Calvert, R. & Snieder, R., 2007a. Improving the virtual source method by wavefield separation, *Geophysics,* **72**(4), V79–V86.

Mehta, K., Snieder, R. & Graizer, V., 2007b. Extraction of near-surface properties for a lossy layered medium using the propagator matrix, *Geophys. J. Int.,* **169,** 271–280.

Menke, W., 1989. *Geophysical Data Analysis,* Academic Press, San Diego.

Miller, D., Oristaglio, M. & Beylkin, G., 1987. A new slant on seismic imaging: migration and integral geometry, *Geophysics,* **52,** 943–964.

Minato, S., Matsuoka, T., Tsuji, T., Draganov, D., Hunziker, J. & Wapenaar, K., 2011. Seismic interferometry using multidimensional deconvolution and crosscorrelation for crosswell seismic reflection data without borehole sources, *Geophysics,* **76**(1), SA19–SA34.

Miyazawa, M., Snieder, R. & Venkataraman, A., 2008. Application of seismic interferometry to extract P- and S-wave propagation and observation of shear-wave splitting from noise data at Cold Lake, Alberta, Canada, *Geophysics,* **73**(4), D35–D40.

Moser, J., Poupon, M., Meyer, H.-J., Wojcik, C., Rosenquist, M., Adejonwo, A. & Smit, D., 2006. Integration of electromagnetic and seismic data to assess residual gas risk in the toe-thrust belt of deepwater Niger Delta, *Leading Edge,* **25**(8), 977–982.

Muijs, R., Robertsson, J.O.A. & Holliger, K., 2007. Prestack depth migration of primary and surface-related multiple reflections. Part I: imaging, *Geophysics,* **72**(2), S59–S69.

van der Neut, J. & Bakulin, A., 2009. Estimating and correcting the amplitude radiation pattern of a virtual source, *Geophysics,* **74**(2), SI27–SI36.

van der Neut, J. & Thorbecke, J., 2009. Resolution function for controlled-source seismic interferometry: a data-driven diagnosis, in *Proc. 79th Annual Int. Meeting Soc. Expl. Geophys., Expanded Abstracts,* pp. 4090–4094, SEG, Tulsa, OK.

van der Neut, J. & Wapenaar, K., 2009. Controlled-source elastodynamic interferometry by cross-correlation of decomposed wavefields, in *EAGE, Extended Abstracts,* X044-1–X044-4, EAGE, Houten.

van der Neut, J., Ruigrok, E., Draganov, D. & Wapenaar, K., 2010. Retrieving the earth's reflection response by multi-dimensional deconvolution of ambient seismic noise, in *EAGE, Extended Abstracts,* P406-1–P406-4, EAGE, Houten.

van der Neut, J., Thorbecke, J., Mehta, K., Slob, E. & Wapenaar, K., 2011. Controlled-source interferometric redatuming by cross-correlation and multi-dimensional deconvolution in elastic media, *Geophysics,* in press.

Nolet, G., 1975. Higher Rayleigh modes in Western Europe, *Geophys. Res. Lett.,* **2,** 60–62.

Norton, S.J., 1992. Annular array imaging with full-aperture resolution, *J. acoust. Soc. Am.,* **92,** 3202–3206.

Oristaglio, M.L., 1989. An inverse scattering formula that uses all the data, *Inverse Probl.,* **5,** 1097–1105.

Picozzi, M., Parolai, S., Bindi, D. & Strollo, A., 2009. Characterization of shallow geology by high-frequency seismic noise tomography, *Geophys. J. Int.,* **176,** 164–174.

Porter, R.P., 1970. Diffraction-limited, scalar image formation with holograms of arbitrary shape, *J. Opt. Soc. Am.,* **60,** 1051–1059.

Riley, D.C. & Claerbout, J.F., 1976. 2-D multiple reflections, *Geophysics,* **41,** 592–620.

Ruigrok, E., Campman, X., Draganov, D. & Wapenaar, K., 2010. High-resolution lithospheric imaging with seismic interferometry, *Geophys. J. Int.,* **183,** 339–357.

Sabra, K.G., Gerstoft, P., Roux, P., Kuperman, W.A. & Fehler, M.C., 2005a. Surface wave tomography from microseisms in Southern California, *Geophys. Res. Lett.,* **32,** L14311-1–L14311-4.

Sabra, K.G., Gerstoft, P., Roux, P., Kuperman, W.A. & Fehler, M.C., 2005b. Extracting time-domain Green's function estimates from ambient seismic noise, *Geophys. Res. Lett.,* **32,** L03310, doi:10.1029/2004GL021862.

Sánchez-Sesma, F.J., Pérez-Ruiz, J.A., Campillo, M. & Luzón, F., 2006. Elastodynamic 2D Green function retrieval from cross-correlation: canonical inclusion problem, *Geophys. Res. Lett.,* **33,** L13305, doi:10.1029/2006GL026454.

Schalkwijk, K.M., Wapenaar, C.P.A. & Verschuur, D.J., 2003. Adaptive decomposition of multicomponent ocean-bottom seismic data into downgoing and upgoing P- and S-waves, *Geophysics,* **68,** 1091–1102.

Schuster, G.T., 2009. *Seismic Interferometry,* Cambridge University Press, Cambridge.

Schuster, G.T. & Hu, J., 2000. Green's function for migration: continuous recording geometry, *Geophysics,* **65,** 167–175.

Schuster, G.T. & Zhou, M., 2006. A theoretical overview of model-based and correlation-based redatuming methods, *Geophysics,* **71**(4), SI103–SI110.

Shapiro, N.M. & Campillo, M., 2004. Emergence of broadband Rayleigh waves from correlations of the ambient seismic noise, *Geophys. Res. Lett.,* **31,** L07614, doi:10.1029/2004GL019491.

Shapiro, N.M., Campillo, M., Stehly, L. & Ritzwoller, M.H., 2005. High-resolution surface-wave tomography from ambient seismic noise, *Science,* **307,** 1615–1618.

Slob, E. & Wapenaar, K., 2007. GPR without a source: cross-correlation and cross-convolution methods, *IEEE Trans. Geosci. Remote Sens.,* **45,** 2501–2510.

Slob, E., Wapenaar, K. & Snieder, R., 2007. Interferometry in dissipative media: addressing the shallow sea problem for Seabed Logging applications, in *Proc. 77th Annual Int. Meeting Soc. Expl. Geophys., Expanded Abstracts,* pp. 559–563, SEG, Tulsa, OK.

Smith, R.B. *et al*., 2009. Geodynamics of the Yellowstone hotspot and mantle plume: seismic and GPS imaging, kinematics, and mantle flow, *J. Volc. Geotherm. Res.,* **188,** 26–56.

Snieder, R., Sheiman, J. & Calvert, R., 2006a. Equivalence of the virtual-source method and wave-field deconvolution in seismic interferometry, *Phys. Rev. E,* **73,** 066620, doi:10.1103/PhysRevE.73.066620.

Snieder, R., Wapenaar, K. & Larner, K., 2006b. Spurious multiples in seismic interferometry of primaries, *Geophysics,* **71**(4), SI111–SI124.

Snieder, R., Miyazawa, M., Slob, E., Vasconcelos, I. & Wapenaar, K., 2009. A comparison of strategies for seismic interferometry, *Surv. Geophys.,* **30,** 503–523.

Stefani, J., Hampson, G. & Herkenhoff, E.F., 2007. Acquisition using simultaneous sources, in *EAGE, Extended Abstracts,* B006-1–B006-4, EAGE, Houten.

Tanter, M., Thomas, J.-L. & Fink, M., 2000. Time-reversal and the inverse filter, *J. acoust. Soc. Am.,* **108**(1), 223–234.

Thorbecke, J. & Wapenaar, K., 2007. On the relation between seismic interferometry and the migration resolution function, *Geophysics,* **72**(6), T61–T66.

Toxopeus, G., Thorbecke, J., Wapenaar, K., Petersen, S., Slob, E. & Fokkema, J., 2008. Simulating migrated and inverted seismic data by filtering a geologic model, *Geophysics,* **73**(2), T1–T10.

Ursin, B., 1983. Review of elastic and electromagnetic wave propagation in horizontally layered media, *Geophysics,* **48,** 1063–1081.

Vasconcelos, I. & Snieder, R., 2008a. Interferometry by deconvolution. Part 1: theory for acoustic waves and numerical examples, *Geophysics,* **73**(3), S115–S128.

Vasconcelos, I. & Snieder, R., 2008b. Interferometry by deconvolution. Part 2: theory for elastic waves and application to drill-bit seismic imaging, *Geophysics,* **73**(3), S129–S141.

Vasconcelos, I., Snieder, R. & Hornby, B., 2008. Imaging internal multiples from subsalt VSP data - Examples of target-oriented interferometry, *Geophysics,* **73**(4), S157–S168.

van Veldhuizen, E.J., Blacquière, G. & Berkhout, A.J., 2008. Acquisition geometry analysis in complex 3D media, *Geophysics,* **73**(5), Q43–Q58.

Wapenaar, C.P.A. & Berkhout, A.J., 1989. *Elastic Wave Field Extrapolation,* Elsevier, Amsterdam.

Wapenaar, C.P.A., Dillen, M.W.P. & Fokkema, J.T., 2001. Reciprocity theorems for electromagnetic or acoustic one-way wave fields in dissipative inhomogeneous media, *Radio Sci.,* **36,** 851–863.

Wapenaar, K. & Fokkema, J., 2006. Green's function representations for seismic interferometry, *Geophysics,* **71**(4), SI33–SI46.

Wapenaar, K., Fokkema, J., Dillen, M. & Scherpenhuijsen, P., 2000. One-way acoustic reciprocity and its applications in multiple elimination and time-lapse seismics, in *Proc. 70th Annual Int. Meeting Soc. Expl. Geophys., Expanded Abstracts,* pp. 2377–2380, SEG, Tulsa, OK.

Wapenaar, K., Fokkema, J. & Snieder, R., 2005. Retrieving the Green's function in an open system by cross-correlation: a comparison of approaches (L), *J. acoust. Soc. Am.,* **118,** 2783–2786.

Wapenaar, K., Slob, E. & Snieder, R., 2008a. Seismic and electromagnetic controlled-source interferometry in dissipative media, *Geophys. Prospect.,* **56,** 419–434.

Wapenaar, K., van der Neut, J. & Ruigrok, E., 2008b. Passive seismic interferometry by multi-dimensional deconvolution, *Geophysics,* **73**(6), A51–A56.

Wathelet, M.D., Jongmans, D. & Ohrnberger, M., 2004. Surface-wave inversion using a direct search algorithm and its application to ambient vibration measurements, *Near Surface Geophys.,* **2,** 211–221.

Yao, H., van der Hilst, R.D. & de Hoop, M.V., 2006. Surface-wave array tomography in SE Tibet from ambient seismic noise and two-station analysis - I. Phase velocity maps, *Geophys. J. Int.,* **166,** 732–744.

Yao, H., Beghein, C. & van der Hilst, R.D., 2008. Surface-wave array tomography in SE Tibet from ambient seismic noise and two-station analysis - II. Crustal and upper-mantle structure, *Geophys. J. Int.,* **173,** 205–219.

Yu, J., Hu, J., Schuster, G.T. & Estill, R., 2006. Prestack migration deconvolution, *Geophysics,* **71**(2), S53–S62.

Zheng, Y., 2010. Retrieving the exact Green's function by wavefield cross-correlation, *J. acoust. Soc. Am.,* **127**(3), EL93–EL98.

Zheng, Y., He, Y. & Fehler, M.C., 2011. Crosscorrelation kernels in acoustic Green's function retrieval by wavefield correlation for point sources on a plane and a sphere, *Geophys. J. Int.,* **184,** 853–859.

APPENDIX: ANALYTICAL EVALUATION OF THE POINT-SPREAD FUNCTION

We evaluate the interferometric point-spread function, as defined in eq. (29), for the situation of a homogeneous lossless medium (propagation velocity c) and a regular distribution of sources with equal autocorrelation functions $S(t)$ along an open source boundary. For our analysis, we rewrite the sum over the source positions $\mathbf{x}_S^{(i)}$ as an integral along the source boundary $\mathbb{S}_{\rm src}$, hence

$$\Gamma(\mathbf{x}, \mathbf{x}_A, t) = \int_{\mathbb{S}_{\rm src}} u^{\rm in}(\mathbf{x}, \mathbf{x}_S, t) * u^{\rm in}(\mathbf{x}_A, \mathbf{x}_S, -t)\, {\rm d}\mathbf{x}_S, \tag{A1}$$

with $\mathbf{x}$ and $\mathbf{x}_A$ at the receiver boundary $\mathbb{S}_{\rm rec}$. Note that, unlike in eq. (11), the source boundary $\mathbb{S}_{\rm src}$ is not enclosing the receivers, hence, $\Gamma(\mathbf{x}, \mathbf{x}_A, t)$ does not converge to $(\rho c/2)\,\{G(\mathbf{x}, \mathbf{x}_A, t) + G(\mathbf{x}, \mathbf{x}_A, -t)\} * S(t)$. For the following analysis we let $\mathbb{S}_{\rm src}$ and $\mathbb{S}_{\rm rec}$ be two horizontal boundaries, with $\mathbb{S}_{\rm rec}$ a distance Δx_3 below $\mathbb{S}_{\rm src}$. For convenience we consider the 2-D situation, so the boundary integral becomes a line integral along $x_{1,S}$. For the chosen configuration the fields under the integral are shift-invariant, that is, they are only functions of the relative distances $x_1 - x_{1,S}$ and $x_{1,A} - x_{1,S}$, respectively. Similarly, the point-spread function is a function of $x_1 - x_{1,A}$ only. Choosing $x_{1,A} = 0$, eq. (A1) can thus be rewritten as

$$\Gamma(x_1, t) = \int_{-\infty}^{\infty} u^{\rm in}(x_1 - x_{1,S}, \Delta x_3, t) * u^{\rm in}(-x_{1,S}, \Delta x_3, -t)\, {\rm d}x_{1,S}, \tag{A2}$$

where $\Gamma(x_1, t)$ is a short notation for $\Gamma(x_1, 0, t)$, etc. We define the double Fourier transform of a space- and time-dependent function $u(x_1, t)$ as

$$\tilde{u}(k_1, \omega) = \int_{-\infty}^{\infty}\int_{-\infty}^{\infty} \exp\{-j(\omega t - k_1 x_1)\} u(x_1, t)\, {\rm d}t\, {\rm d}x_1. \tag{A3}$$

Hence, eq. (A2) transforms to

$$\tilde{\Gamma}(k_1, \omega) = \tilde{u}^{\rm in}(k_1, \Delta x_3, \omega)\,\{\tilde{u}^{\rm in}(k_1, \Delta x_3, \omega)\}^*. \tag{A4}$$

In Section 4.2, we argued that the representation for MDD [eq. (26)] holds, irrespective of the type of sources at $\mathbb{S}_{\rm src}$. For convenience of the analysis we consider dipole sources emitting a signal $s(t)$ (this is for example representative for the situation of vertically oriented vibrators

at a free surface). The expression for $\tilde{u}^{\mathrm{in}}(k_1, \Delta x_3, \omega)$ is thus given by

$$\tilde{u}^{\mathrm{in}}(k_1, \Delta x_3, \omega) = \hat{s}(\omega) \times \begin{cases} \exp\left\{-j\,\mathrm{sgn}(\omega)\sqrt{k^2 - k_1^2}\,\Delta x_3\right\} & \text{for} \quad k_1^2 \leq k^2 \\ \exp\left\{-\sqrt{k_1^2 - k^2}\,\Delta x_3\right\} & \text{for} \quad k_1^2 > k^2, \end{cases} \tag{A5}$$

with $k = \omega/c$. Substitution into eq. (A4) gives

$$\tilde{\Gamma}(k_1, \omega) = \hat{S}(\omega) \times \begin{cases} 1 & \text{for} \quad k_1^2 \leq k^2 \\ \exp\left\{-2\sqrt{k_1^2 - k^2}\,\Delta x_3\right\} & \text{for} \quad k_1^2 > k^2, \end{cases} \tag{A6}$$

with $\hat{S}(\omega) = |\hat{s}(\omega)|^2$. Hence, for propagating waves ($k_1^2 \leq k^2$) the Fourier-transformed point-spread function $\tilde{\Gamma}(k_1, \omega)$ is equal to the power spectrum $\hat{S}(\omega)$ of the dipole sources, whereas for evanescent waves ($k_1^2 > k^2$) it is exponentially decaying. Note that for the limit $\Delta x_3 \to 0$ the point-spread function approaches $\hat{S}(\omega)$ for all k_1. Hence, for this case we have $\lim_{\Delta x_3 \to 0} \Gamma(x_1, t) = \{\delta(x_1)\delta(t)\} * S(t)$, meaning that the only band-limitation is caused by the autocorrelation of the sources. However, for any realistic value of Δx_3 the exponentially decaying character of the evanescent waves imposes a more serious band-limitation to the delta function. Already for Δx_3 larger than a few wavelengths it is reasonable to approximate the exponentially decaying term in eq. (A6) by zero for all $k_1^2 > k^2$, meaning that for a given frequency ω the passband is $-|\omega|/c \leq k_1 \leq |\omega|/c$. Hence, the inverse transformation to the space-frequency domain is obtained as

$$\begin{aligned} \hat{\Gamma}(x_1, \omega) &= \frac{1}{2\pi} \int_{-\infty}^{\infty} \tilde{\Gamma}(k_1, \omega) \exp(-j k_1 x_1)\, \mathrm{d}k_1 \\ &= \frac{\hat{S}(\omega)}{2\pi} \int_{-|\omega|/c}^{|\omega|/c} \exp(-j k_1 x_1)\, \mathrm{d}k_1 = \frac{\sin(|\omega| x_1/c)}{\pi x_1}\, \hat{S}(\omega). \end{aligned} \tag{A7}$$

Note that this expression is identical to the resolution function for 2-D seismic migration (Berkhout 1984). When the source array is finite, the passband is further reduced to $-|\omega| \sin\alpha_{\max}/c \leq k_1 \leq |\omega| \sin\alpha_{\max}/c$, where $\alpha_{\max}$ is the maximum propagation angle. Hence, for this situation we replace the velocity c in eq. (A7) by the apparent velocity $c_{\mathrm{a}} = c/\sin\alpha_{\max}$.

To obtain the space-time domain expression we first rewrite eq. (A7) as

$$\begin{aligned} \hat{\Gamma}(x_1, \omega) &= -j\,\mathrm{sgn}(\omega)\, \frac{j \sin(\omega x_1/c_{\mathrm{a}})}{\pi x_1}\, \hat{S}(\omega) \\ &= -j\,\mathrm{sgn}(\omega)\, \frac{\exp(j\omega x_1/c_{\mathrm{a}}) - \exp(-j\omega x_1/c_{\mathrm{a}})}{2\pi x_1}\, \hat{S}(\omega). \end{aligned} \tag{A8}$$

This product of three functions in the frequency domain transforms to a convolution of the corresponding time-domain functions, as follows

$$\Gamma(x_1, t) = \frac{1}{\pi t} * \frac{\delta(t + x_1/c_{\mathrm{a}}) - \delta(t - x_1/c_{\mathrm{a}})}{2\pi x_1} * S(t). \tag{A9}$$

For $x_1 \neq 0$ this gives

$$\Gamma(x_1, t) = \frac{1}{2\pi^2 x_1} \left[\frac{1}{t + x_1/c_{\mathrm{a}}} - \frac{1}{t - x_1/c_{\mathrm{a}}}\right] * S(t), \tag{A10}$$

and for $x_1 \to 0$

$$\Gamma(0, t) = \frac{1}{\pi^2 c_{\mathrm{a}} t} * \frac{\partial S(t)}{\partial t}. \tag{A11}$$

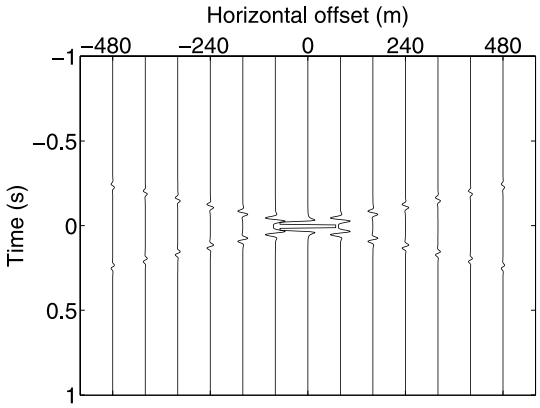

Figure A1. The point-spread function $\Gamma(x_1, t)$ (clipped at 20 per cent of its maximum amplitude) for the situation of a homogeneous lossless medium (propagation velocity 2000 m s^{-1}) and an infinite regular source array. The autocorrelation of the sources is a Ricker wavelet with a central frequency of 20 Hz.

$\Gamma(x_1, t)$ is illustrated in Fig. A1 for $c = 2000$ m s^{-1}, $\alpha_{\max} = \pi/2$ (corresponding to an infinite source array) and $S(t)$ a Ricker wavelet with a central frequency of 20 Hz. Note that $\Gamma(x_1, t)$ reveals an X-pattern with the maximum amplitude at $(x_1, t) = (0, 0)$ and decaying amplitudes along lines $t = \pm x_1/c$. The point-spread function $\Gamma(x_1, t)$ can be seen as a band-limited delta function $\delta(x_1)\delta(t)$, with the temporal band-limit imposed by the autocorrelation function $S(t)$ and the spatial band-limit imposed by the evanescent waves and, for a finite source array, the absence of large propagation angles.

For the derivation in this appendix we considered a 2-D configuration and assumed the sources are dipoles. For other situations (3-D configuration and/or monopole sources) the details are different, but in all cases the analytical point-spread function reveals the characteristic X-pattern (or a two-sided conical pattern in 3-D).